buildings

MDPI

Article

Energy Cascade Utilization in a Building-Integrated Photovoltaic–Thermal Catalytic-Dehumidification System for Indoor Environment Regulation

Jing Li [1], Wenluo Li [1], Weikai Wang [1], Feng Zheng [1], Niansi Li [1], Jie Ji [2] and Bendong Yu [1,*]

[1] College of Urban Construction, Nanjing Tech University, Nanjing 210009, China
[2] Department of Thermal Science and Energy Engineering, University of Science and Technology of China, Hefei 230026, China
* Correspondence: yubendonglns@163.com

Abstract

The conflict between building operational energy consumption and indoor environmental quality (IEQ) presents a critical challenge in sustainable building design. To address this, we propose a building-integrated photovoltaic–thermal catalytic-dehumidification (PV-TC/DH) system that achieves energy cascade utilization through a "purification-first, dehumidification-second" series configuration. The key feature is the cascaded use of solar thermal energy: PV-generated low-grade heat (~40–60 °C) is first used to raise the temperature of the α-MnO_2 thermal catalyst and to preheat the airflow, after which the heated airflow transfers its remaining sensible heat to the downstream MIL-101(Cr) layer for MOF regeneration; the adsorption heat released during night-time MOF operation provides a further, moisture-limited heating contribution. The same low-grade heat raises the operating temperature of the α-MnO_2 catalytic layer, and the catalyst is active at low temperature in its own right; because the fitted activation energy is only 6.78 kJ/mol, the additional rate gained between 10 and 50 °C is modest (of order 20%), and the larger benefit of the heat lies in the regeneration of the downstream MOF layer. A transient heat and mass transfer model, validated separately for the PV-TC wall and for the PV-DH roof, was developed, and a multi-objective optimization framework (NSGA-II combined with TOPSIS) was established to identify balanced configurations. For the reference configuration in Nanjing, the simulated annual photovoltaic generation is 4532 kWh and the annual clean-air delivery is 276,129 m^3; the annual dehumidification totals are not compared between cities, because the daily and annual accumulations have not been reconciled. In Nanjing the simulated cooling and heating outputs amount to 600 kWh and 665 kWh per year; these quantities are not season-matched and are therefore reported as energy outputs rather than as demonstrated load reductions, and the simple payback period of 2.5 years is a static estimate in which the sorbent is costed at the material cost of MIL-101(Cr) synthesized in our laboratory, so it remains an order-of-magnitude indication rather than a demonstrated economic case. The optimization suggests that design parameters may need to be adapted to local solar availability and humidity, but the resulting preferences are provisional, since several optima lie on the prescribed bounds. The results are model predictions for a prescribed operating sequence: no room-level heat and moisture balance was solved, so indoor thermal comfort, indoor humidity and occupant exposure are not quantified. The work indicates that building-integrated energy cascade systems can reduce the operational energy demand of an envelope, and offers an indicative pathway towards low-energy buildings rather than a demonstrated route to net-zero-energy buildings.

Check for updates

Academic Editor: Vincenzo Costanzo

Received: 11 October 2026
Revised: 17 November 2026
Accepted: 25 November 2026
Published: 29 November 2026

Copyright: © 2026 by the authors. Licensee MDPI, Basel, Switzerland. This article is an open access article distributed under the terms and conditions of the Creative Commons Attribution (CC BY) license.

Keywords: building-integrated system; energy cascade utilization; photovoltaic–thermal catalysis; MOF dehumidification; multi-objective optimization

1. Introduction

The building sector accounts for approximately 30% of global final energy consumption and is responsible for a significant share of carbon emissions [1,2]. Meanwhile, people spend 80–90% of their time indoors, making indoor environmental quality (IEQ)—encompassing thermal comfort, air cleanliness, and humidity levels—a critical determinant of occupant health and productivity [3–5]. However, achieving a balanced improvement in energy generation and indoor environmental regulation remains challenging because multiple performance objectives are often coupled and conflicting within integrated building systems. These two objectives are inherently coupled: maintaining ideal indoor conditions traditionally relies on energy intensive heating, ventilation, and air conditioning (HVAC) systems. As the global community pursues carbon neutrality targets, there is an urgent need for innovative building envelope technologies that can simultaneously reduce operational energy consumption and deliver healthy indoor environments.

Among the various IEQ parameters, airborne volatile organic compounds (VOCs)—particularly formaldehyde—and excessive humidity are of paramount concern. Long-term exposure to formaldehyde, even at sub ppm concentrations, has been linked to respiratory diseases and impaired immune function [4–7], while high humidity promotes mold proliferation and accelerates building material degradation [8–12]. Conventional approaches to these challenges include adsorption, photocatalytic oxidation, and condensation dehumidification [9–11,13–16]. However, each technology has inherent limitations. Adsorption-based purification generally requires periodic regeneration or replacement of adsorbents and may generate secondary waste. Photocatalytic oxidation is constrained by catalyst activity and spectral utilization, particularly under low-temperature and low-light conditions [14,15,17,18]. Condensation dehumidification relies on vapor-compression refrigeration and therefore involves substantial electricity consumption, limiting its suitability for energy-efficient building applications [12,16,19,20]. These limitations highlight the need for integrated approaches that can utilize renewable or otherwise available thermal energy to simultaneously address air purification and humidity control.

Previous studies have explored several relevant approaches for solar-assisted indoor environmental regulation. For photovoltaic– and solar–thermal catalytic purification, manganese oxide-based catalysts and building-integrated thermal-catalytic walls have been investigated for indoor formaldehyde removal and thermal management [21–24]. More recently, a photothermal/radiative-cooling thermal-catalytic hybrid system was proposed to combine daytime solar energy harvesting with night-time radiative cooling for indoor environment improvement [25]. These studies demonstrate the potential of solar-driven thermal catalysis, while their primary focus is catalytic purification and associated thermal management. In parallel, extensive research has been conducted on MOF-based moisture adsorption, including water sorption characteristics, adsorption kinetics, thermodynamic properties, and their application in dehumidification heat exchangers [26–32]. Solar-assisted desiccant cooling and photovoltaic-driven day–night moisture management have also been investigated [13,33]. Furthermore, solar heating combined with nocturnal radiative cooling has been explored for diurnal heat collection and thermal regulation [34–37]. Although these studies provide important foundations for the individual functions involved, they employ different system configurations and moisture-control mechanisms from those considered in the present work. Accordingly, the contribution of the present study is not the

independent introduction of thermal catalysis, MOF adsorption, or radiative cooling. Rather, it lies in integrating these functions into a series-connected building envelope system, in which an upstream photovoltaic–thermal catalytic wall is coupled with a downstream MOF-based dehumidification roof. The interaction between the two modules further enables the sequential utilization of PV-generated low-grade heat for thermal catalytic purification, airflow preheating, and subsequent MOF regeneration. The distinction between representative previous studies and the present system is summarized in Table 1.

Table 1. Comparison of representative previous studies and the present work.

Research Category	Main Focus of Representative Studies	Difference from the Present Work
Solar-thermal catalytic purification [21–24]	Solar-assisted low-temperature thermal catalysis, catalytic Trombe walls, and catalytic purification systems incorporating thermal storage.	Primarily focus on catalytic purification and thermal management, rather than a serial air-treatment pathway combining catalytic purification with downstream MOF adsorption dehumidification.
Photothermal/radiative-cooling thermal catalysis [25]	Integration of solar photothermal heating, nocturnal radiative cooling, and thermal catalytic purification.	Demonstrates the combination of radiative cooling and thermal catalysis, whereas the present study further integrates a downstream MIL-101(Cr)-based adsorption dehumidification unit and coordinates its regeneration with PV thermal energy.
MOF-based adsorption dehumidification [26–28]	Water-vapor adsorption characteristics, adsorption kinetics, thermodynamics, and MOF-based dehumidification, including heat-exchanger coating applications.	Focus on adsorbent materials and dehumidification processes; the present study couples the MOF adsorber with an upstream PV-thermal catalytic purification module.
Solar/PV-assisted dehumidification [13,33]	PV/T-assisted desiccant cooling and photovoltaic-driven moisture evaporation and absorption for day–night power generation and dehumidification.	Employ different dehumidification mechanisms and system configurations from the MIL-101(Cr) adsorption stage integrated with α-MnO_2 catalytic air purification in the present work.
Solar heating and nocturnal radiative cooling [34–37]	Daytime solar heat collection and night-time radiative cooling for diurnal thermal regulation.	Focus on heat/cold collection and thermal management, without the specific integration of catalytic purification and MOF-based moisture adsorption/regeneration proposed here.
Present PV-TC/DH system	Series-connected α-MnO_2 PV-TC wall and MIL-101(Cr)-based PV-DH roof; sequential PV heat utilization; coordinated daytime regeneration and night-time adsorption; climate-adaptive optimization.	Integrates electricity generation, formaldehyde purification, moisture removal, and low-grade thermal energy utilization within a coordinated building-envelope system.

To address these challenges, this study proposes a building-integrated photovoltaic thermal-catalytic/dehumidification (PV-TC/DH) hybrid system consisting of a photovoltaic thermal-catalytic wall (PV-TC wall) and a photovoltaic-driven dehumidification roof (PV-DH roof) connected in series. Unlike systems that independently perform air purification and dehumidification, the proposed configuration establishes a sequential indoor air-treatment pathway. Indoor air first passes through the PV-TC wall, where formaldehyde is removed through thermal catalytic oxidation over the α-MnO_2-coated surface. The pretreated air then enters the PV-DH roof, where water vapor is adsorbed by the MIL-101(Cr)-coated finned-tube heat exchanger. The proposed configuration further enables the cascaded utilization of low-grade thermal energy generated by the PV modules. During daytime operation, PV-generated heat is first used to maintain the operating temperature of

the α-MnO_2 thermal-catalytic layer and preheat the airflow. The remaining sensible heat carried by the preheated airflow is subsequently transferred to the downstream MIL-101(Cr) adsorbent to support desorption and regeneration. During suitable night-time conditions, radiative cooling reduces the temperature of the PV-DH adsorption unit, promoting moisture adsorption by MIL-101(Cr). Seasonal operating strategies are also implemented to accommodate different thermal and humidity demands, including the utilization of MOF adsorption heat for auxiliary heating during winter night-time operation. To investigate the coupled performance of the proposed system, a transient heat and mass transfer model was developed and experimentally validated to characterize photovoltaic conversion, thermal transfer, airflow, VOC degradation, and MOF adsorption/desorption processes. Furthermore, considering the competing objectives of photovoltaic electricity generation, clean air production, and dehumidification capacity, a multi-objective optimization framework integrating the non-dominated sorting genetic algorithm II (NSGA-II) and the Technique for Order Preference by Similarity to Ideal Solution (TOPSIS) was developed to identify balanced system configurations. The optimized performance was further investigated under different climatic conditions in Beijing, Nanjing, Shenzhen, and Xining. The key contributions of this study can be summarized as follows: (1) Series-connected integration of air purification and dehumidification. A building-integrated PV-TC/DH system is developed by connecting an α-MnO_2-based photovoltaic thermal-catalytic wall and a MIL-101(Cr)-based photovoltaic dehumidification roof in series. This configuration establishes a sequential "purification-first, dehumidification-second" air-treatment pathway, enabling the coordinated removal of gaseous formaldehyde and water vapor. (2) Cascaded utilization of PV-generated low-grade thermal energy. The thermal energy recovered from the PV modules is sequentially utilized to maintain the operating temperature of the upstream thermal-catalytic layer and preheat the airflow. The remaining sensible heat carried by the preheated air is subsequently used to drive the desorption and regeneration of the downstream MIL-101(Cr) adsorbent. This arrangement improves the utilization of PV-generated thermal energy across different functional stages. (3) Coordinated day–night and seasonal operation. During daytime operation, solar energy supports photovoltaic electricity generation, thermal-catalytic purification, and MOF regeneration. During suitable night-time conditions, radiative cooling reduces the temperature of the PV-DH adsorption unit, promoting water-vapor adsorption by MIL-101(Cr). In winter, the operating strategy suppresses unnecessary radiative heat loss and utilizes the heat released by MOF adsorption for auxiliary indoor heating. (4) Climate-adaptive multi-objective optimization. A multi-objective optimization framework combining NSGA-II and TOPSIS is established to balance photovoltaic electricity generation, clean air production, and dehumidification capacity. The proposed framework is applied to different climatic regions to identify suitable system configurations and operating strategies.

2. System Description

2.1. Basic Structure

Figure 1 schematically illustrates the proposed building-integrated hybrid system, which synergistically couples photovoltaic thermal catalysis with dehumidification to enable concurrent power generation and air treatment across the cooling and heating seasons. The system consists of two principal components: a photovoltaic thermal catalytic ventilation wall and a photovoltaic-driven, MOF-based dehumidification roof. The two modules are interconnected via an air channel, with their interior-side flow paths configured in series through controllable dampers. This series configuration forms the foundation for functional synergy, allowing one module to precondition the airstream and thereby enhance the performance of the other. It should be clarified at the outset that the experiments

reported in this study were performed on the two components separately, namely the PV-TC wall and the MIL-101(Cr)-coated finned-tube module, whereas the behavior of the series-connected system as a whole was obtained from the coupled numerical model described in Section 3. The system-level results reported in Section 4 are therefore model predictions built on component-validated sub-models rather than measurements on a fully integrated prototype.

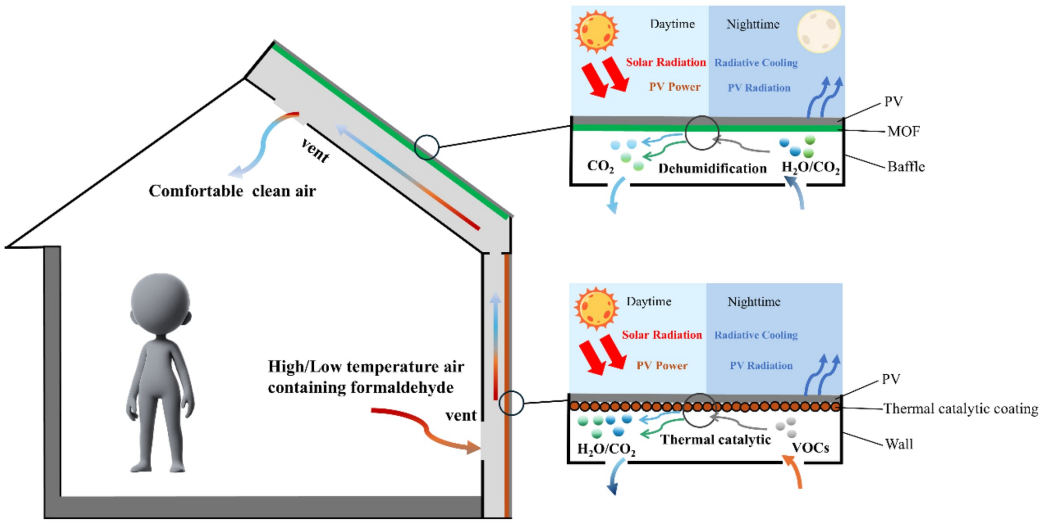


Figure 1. Schematic diagram of the PV-TC/DH system, showing the upstream photovoltaic thermal-catalytic wall, the downstream photovoltaic-driven MIL-101(Cr) dehumidification roof, the series air path connecting the two modules, and the airflow directions in the two modules.

The backplate of the PV-TC wall is coated with a low-temperature α-MnO_2 thermal-catalytic layer, which facilitates the oxidation of gaseous formaldehyde and other VOCs into CO_2 and H_2O. The PV-DH roof incorporates a finned-tube heat exchanger coated with MIL-101(Cr), which serves as the water-vapor adsorption and desorption component. The finned-tube configuration provides an extended heat-transfer surface for thermal exchange between the airflow and the MOF coating. Both modules utilize spectrally selective photovoltaic panels designed to achieve high solar absorptivity for daytime photovoltaic conversion and photovoltaic thermal harvesting, together with high emissivity within the atmospheric window to facilitate nocturnal radiative cooling. During operation, indoor air is first drawn into the PV-TC wall channel, where it is thermally conditioned by the photovoltaic backplate while formaldehyde undergoes catalytic oxidation over the α-MnO_2 layer. The pretreated air subsequently passes into the PV-DH roof channel, where water vapor is adsorbed by the MIL-101(Cr) coating on the finned-tube heat exchanger. Finally, the treated air, with reduced formaldehyde and moisture contents, is recirculated into the indoor space. This "purification-first, dehumidification-second" configuration establishes a sequential air-treatment process and enables functional coordination between the two modules. For example, during summer days, the PV-TC wall preheats the air, significantly enhancing the regeneration efficiency of the MOF layer in the PV-DH roof. At night, the PV-TC wall precools the air, thereby enhancing the adsorption capacity of the PV-DH roof and enabling deeper dehumidification.

The system achieves spatiotemporal coordination and cascaded utilization of PV-generated thermal energy. During daytime operation, the low-grade heat recovered from the PV modules is first used to maintain the operating temperature of the α-MnO_2 thermal-catalytic layer and preheat the airflow in the PV-TC wall. The preheated airflow then enters the downstream PV-DH roof, where its remaining sensible heat is transferred to the MIL-

101(Cr)-coated finned-tube heat exchanger to support moisture desorption and adsorbent regeneration. Thus, the thermal energy generated by the PV modules is sequentially utilized by the thermal-catalytic and dehumidification stages. The effectiveness of this coordinated energy cascade is dependent on the availability of solar thermal energy and the thermal conditions of the airflow entering the downstream dehumidification module. During periods of insufficient solar radiation, the thermal energy available for catalytic temperature maintenance and MOF regeneration may decrease. Similarly, elevated night-time ambient temperatures and unfavorable atmospheric conditions may weaken the radiative cooling potential and consequently reduce the adsorption capacity of MIL-101(Cr). Prolonged high-humidity conditions may also increase the moisture loading of the adsorbent and place greater demands on daytime regeneration. Therefore, the coordinated operating strategy is intended to improve the utilization of available solar and radiative thermal resources under suitable climatic conditions, rather than guarantee constant performance under all weather conditions. The cascade described here should be understood as a sequential use of the sensible heat carried by the airflow and of the solar heat absorbed by each module, rather than as a thermodynamic cascade with a quantified exergy budget: the catalytic layer is a temperature-activated function and does not consume the thermal energy supplied to it. An exergy balance for each stage, and a comparison between the coupled configuration and independently operated modules of equal collector area and equal airflow, have not been carried out in the present work, and the comparison in Section 4.1 is accordingly made against single-module systems whose collector areas differ from that of the integrated system.

In this study, the term "energy cascade utilization" refers to the sequential use of PV-generated low-grade thermal energy for thermal-catalytic purification, airflow preheating, and subsequent MOF regeneration. It does not refer to the secondary utilization of heat released by the formaldehyde oxidation reaction. The night-time operating strategy varies according to seasonal conditions. During suitable summer night-time conditions, radiative cooling reduces the temperature of the PV-DH adsorption unit, thereby improving the water-vapor adsorption performance of the MIL-101(Cr) coating. During winter night-time operation, the PV-TC wall is deactivated and unnecessary radiative heat loss from the roof-mounted PV panels is suppressed. Meanwhile, indoor air passes through the PV-DH roof, where MIL-101(Cr) adsorbs water vapor and releases adsorption heat. The resulting warm and dehumidified air is returned to the indoor space, providing auxiliary heating and humidity regulation. Through this coordinated operation, the proposed system integrates photovoltaic electricity generation, thermal-catalytic air purification, and adsorption-based dehumidification while improving the utilization of available low-grade thermal energy across different operating periods.

2.2. Operation Mode

To adapt to the dynamically changing outdoor climate and varying indoor environmental demands throughout the year, the proposed hybrid system incorporates a rule-based, multi-mode operational strategy. This strategy flexibly switches air flow paths and functional priorities by controlling the open/closed states of ventilation ports and internal connecting dampers in each module. Consequently, it enables adaptive adjustment among various operational scenarios, such as summer cooling/dehumidification, winter heating/purification, and transitional season ventilation/insulation, thereby optimizing both energy efficiency and indoor environmental quality. The specific operational modes are illustrated in Figure 2, primarily categorized into the following four typical scenarios.

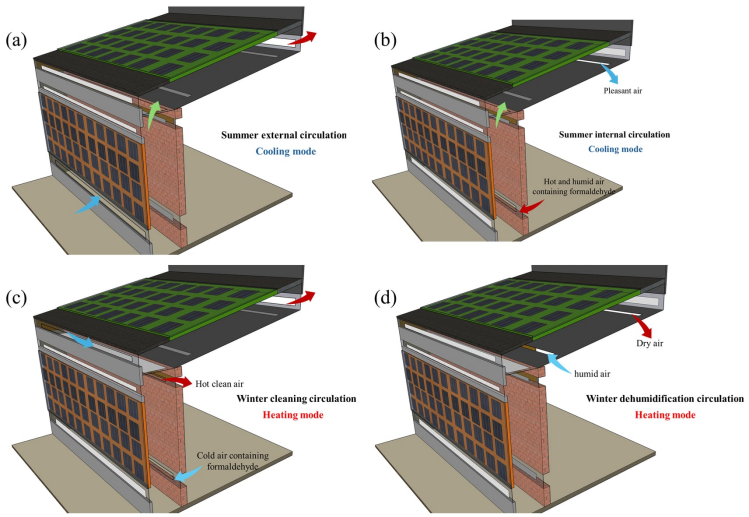


Figure 2. Operation modes of the system: (**a**) Summer external circulation. (**b**) Summer internal circulation. (**c**) Winter cleaning circulation. (**d**) Winter dehumidification circulation.

The transition among these four modes is realized by the open or closed states of the indoor and outdoor vents of each module and of the connecting damper between them, together with the operation of the supply fan. In the present, the energy required for actuation, for the fan, and for the deployment of the roof cover in winter is not included in the reported energy balances. The use of measured indoor temperature and humidity as control inputs, and the optimization of the switching thresholds themselves, are not investigated here.

The switching sequence used in the simulation is a single rule-based schedule rather than a set of alternative control laws: the vents, dampers and fans are set to the external-circulation configuration during the daylight window (09:00–17:00 local time for Beijing, Nanjing and Shenzhen, and 10:00–18:00 for Xining) and to the internal-circulation configuration for the remaining hours, with the winter-night roof cover deployed throughout the night. The schedule is open-loop, that is, it does not use measured indoor temperature or humidity, and the switching thresholds themselves were not optimized.

During summer daytime operations, to keep the occupied space out of the outdoor air path during the cooling season and to use the abundant solar thermal energy for regenerating the desiccant material, the system closes all indoor vents, opens outdoor vents, and configures the PV-TC wall and PV-DH roof airflow passages in series. Driven by a fan, outdoor air enters the PV-TC wall inlet and is thermally heated via solar irradiation through the PV-TC wall, resulting in a marked temperature rise. The preheated air subsequently enters the PV-DH roof's flow passage. The sensible thermal energy carried by the airflow, together with the solar thermal input directly absorbed by the roof module, increases the thermal driving force for moisture desorption and MOF regeneration. Therefore, the thermal energy generated by the PV system is sequentially utilized by the upstream thermal catalytic stage and the downstream dehumidification stage, thereby improving moisture desorption and regeneration efficiency of the MOF adsorption layer in the PV-DH roof channel and preserving adsorption capacity for night-time dehumidification. This mode treats outdoor air only; the occupied space is isolated from the outdoor air path, so the heat load that ventilating with untreated outdoor air would impose is avoided, while regeneration and power generation proceed. Notably, the PV-TC wall's preheating effect further augments the PV-DH roof's regeneration efficiency. The regeneration effectiveness is influenced by the available solar thermal input and the temperature of the preheated airflow. Under reduced solar radiation, the thermal driving force for MOF desorption may

become insufficient to achieve the same regeneration level as that under favorable daytime conditions. It should be explicitly clarified that during this summer daytime external circulation mode, the system's primary function is MOF regeneration and photovoltaic power generation. The system does not process indoor air, nor does it supply conditioned fresh air or purify indoor formaldehyde during this specific period.

During summer night-time, the system opens all indoor ventilation ports, closes outdoor ports, and activates the connecting damper between the PV-TC wall and the PV-DH roof, establishing a series-connected air duct. Warm, humid indoor air, driven by buoyancy forces or low-power auxiliary fans, first passes through the PV-TC wall. The PV panels radiate heat to cold outer space through the atmospheric transparency window, thereby cooling the air within the flow channel. Concurrently, the catalytic layer continues to operate, although its conversion is lower than that obtained at the elevated temperatures used during daytime operation. Subsequently, the air enters the flow channel of the PV-DH roof, where it undergoes additional cooling via the radiative cooling effect. The adsorption capacity of the MOF material is substantially enhanced at reduced temperatures, enabling deep air dehumidification. Ultimately, conditioned air that is cool, dry, and purified is recirculated back into the indoor space. This operating mode utilizes night-time radiative cooling to reduce the temperature of the airflow and the MOF adsorption unit, thereby promoting moisture adsorption and providing passive cooling under favorable atmospheric conditions. The actual cooling and dehumidification performance depends on the night-time ambient temperature, atmospheric conditions, and available airflow. Auxiliary fan power may still be required depending on the operating conditions. This night-time operation functions as an internal circulation mode, where indoor air is purified and dehumidified without fresh air intake.

During winter daytime, the system opens the indoor ventilation port of the PV-TC wall while closing its connecting damper to the PV-DH roof, creating an independent indoor air circulation loop. Cold indoor air enters the PV-TC wall flow channel, where it is heated by the solar thermal energy harvested by the PV panels. This elevates the supply air temperature and simultaneously provides the optimal thermal conditions required for the photovoltaic thermal layer to decompose formaldehyde, yielding the dual benefits of space heating and air purification. Concurrently, the PV-DH roof circulates outdoor air, utilizing harvested solar thermal energy to regenerate the MOF layer in preparation for subsequent night-time dehumidification demands, while continuously producing electrical power. Notably, during this operational phase, the PV-TC wall provides active heating to the indoor space. When the PV-TC wall subsequently ceases operation, the PV-DH roof assumes the heating duty via adsorption heat release. The availability of sufficient daytime solar thermal energy is important for restoring the adsorption capacity of the MOF adsorbent before the subsequent night-time operation. Therefore, the regeneration performance may vary with the local solar radiation and the preceding adsorption history.

During winter night-time, the system closes all ventilation ports of the PV-TC wall, deactivating it to minimize conductive and convective heat loss from the indoor space through the wall assembly. To mitigate the radiative cooling effect that would otherwise reduce the surface temperature of the PV modules and degrade indoor thermal comfort, the roof-mounted PV panels are covered, effectively suppressing radiative heat emission to the night sky. Meanwhile, the PV-DH roof opens its indoor ventilation port. Indoor air flows through the PV-DH roof flow channel, where the MOF layer adsorbs atmospheric moisture and releases significant quantities of adsorption heat, thereby elevating the air temperature. This warm, dehumidified air is recirculated back into the indoor environment, achieving passive heating and humidity regulation without a separate heat source, although the fan, damper and cover actuation power of this mode is not included in the reported

energy balances. When the PV-DH roof requires regeneration, the PV-TC wall resumes indoor air circulation, utilizing stored solar photovoltaic thermal energy to provide heating and air purification. This coordinated handover between the two modules provides a potential for extended night-time heating and humidity regulation. However, the duration and effectiveness of this operation depend on the available MOF adsorption capacity, the heat released during moisture uptake, and the regeneration achieved during the preceding daytime period. In the simulation the roof cover is assumed to be fully deployed throughout the winter night, and the energy required for its deployment, for the fans and for damper actuation is not included in the reported energy balances.

Additionally, it should be noted that during night-time operation, the system operates in an internal circulation mode to recirculate and treat indoor air. The accumulation of occupant-generated CO_2 and moisture during this closed-loop operation was not explicitly modeled in the current study, as the model assumes a fixed inlet formaldehyde concentration and focuses on thermal, catalytic, and dehumidification performance. In practical applications, maintaining acceptable indoor CO_2 levels requires periodic fresh air exchange or integration with a dedicated outdoor air system (DOAS). Future research should couple the system with dynamic occupancy schedules and indoor air quality (IAQ) models to comprehensively evaluate the CO_2 accumulation and occupant moisture impacts.

This dynamic, multi-mode operational strategy, which is based on seasonal and diurnal variations, is intended to allow the system to adapt to building environmental demands over the annual cycle. It combines several physical and chemical processes, including photovoltaic thermal conversion, radiative cooling, photovoltaic power generation, thermal catalytic oxidation, and adsorptive dehumidification. The strategy is rule-based, and its performance is evaluated here under typical meteorological conditions for a prescribed operating sequence. The extent to which it can maintain acceptable indoor conditions under all operating conditions has not been demonstrated, and requires both whole-building simulation and long-term integrated testing.

3. Research Methodology

3.1. System Model Establishing

The system model consists of coupled heat and mass transfer sub models. The heat transfer sub model comprises three distinct components: the PV panels integrated into both the PV-TC wall and the PV-DH roof, the interconnected air flow channels, and the underlying PV-DH roof structural assembly. The mass transfer sub model describes the thermal catalytic oxidation process of formaldehyde within the air flow channels and the reversible adsorption–desorption processes of water vapor on the MOF sorbent (Figure 3). To facilitate mathematical tractability and simplify numerical analysis, the following reasonable assumptions are adopted: (1) The PV panels, air within the flow channels, and PV-DH roof assembly are modeled as one-dimensional heat and mass transfer media; (2) The temperature, emissivity, and transmittance of the PV surface are assumed to be spatially uniform; (3) Only temperature gradients along the air flow direction are considered; temperature gradients through the thickness of the PV panels are neglected; (4) The temperature of the photovoltaic thermal layer is assumed to be identical to that of the underlying PV panel, owing to the nanoscale thickness of the α-MnO_2 coating [38]; (5) Heat released by the photovoltaic thermal oxidation reaction is neglected, as formaldehyde concentrations in typical indoor environments are extremely low [15,39].

In the equations that follow, the convective heat exchange between a solid layer and the channel air appears as a sink in the balance of the solid layer and as an equal source in the balance of the air, so that the coupled formulation is energy conserving. Only conduction in the direction of the airflow is retained in each layer, consistent with assumption (3); the wall assembly is represented by a single homogeneous layer, and no lateral conduction term is included in the module balances. The solar term denotes the irradiance absorbed by the surface rather than the incident irradiance, and the optical properties listed in Section 3.3 are the effective absorptance and emittance of the coated surfaces.

The ambient air temperature is denoted T_amb in all balances; the symbol T_abm that appeared in Equations (1) and (12) of the previous version has been replaced by T_amb, and the bulk-mean temperature of the moist air is denoted T_a. Conduction across the wall thickness is not resolved in the module balance: the wall is represented by a single lumped layer, and the term $\lambda_w\delta_w\partial^2T_w/\partial y^2$ retained in Equations (1), (12) and (17) of the previous version has been removed accordingly, consistent with assumption (3).

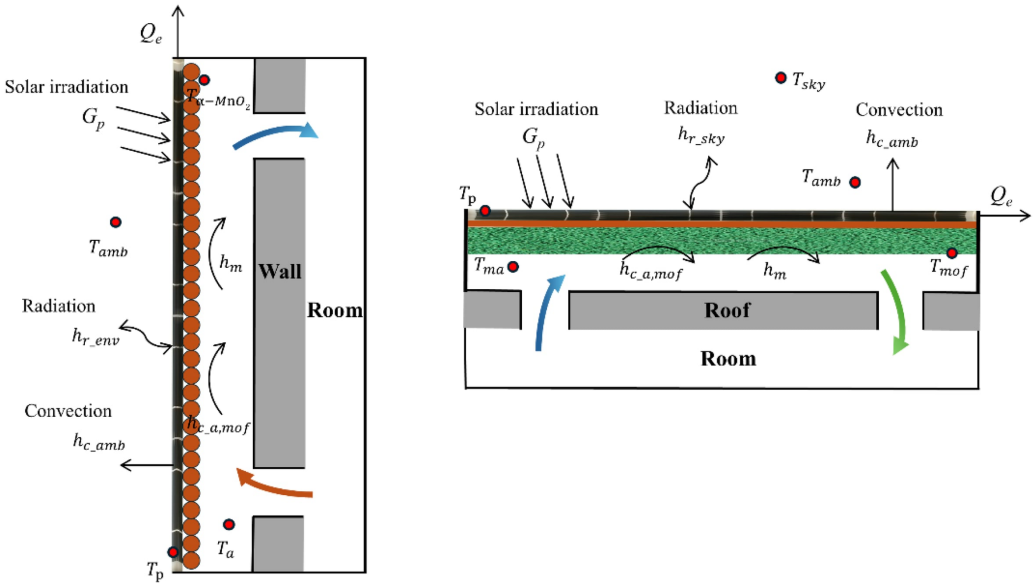


Figure 3. The schematic diagram of heat and mass transfer of the PV-TC/DH system.

3.1.1. Heat-Balance Equation of PV-TC Wall

For the PV cell of wall, owing to its very small thickness, heat conduction across the cell thickness is neglected and only the axial heat transfer along the flow direction is retained; and the corresponding heat balance reads as:

$$\rho_p\delta_p c_p\frac{\partial T_p}{\partial t} = G_p - Q_e + h_{c_abm}\left(T_{amb} - T_p\right) + h_{r_env}\left(T_{amb} - T_p\right) + \frac{k_p}{\delta_p}\left(T_{\alpha-MnO_2} - T_p\right) \quad (1)$$

where ρ_p denotes the density of the PV cell (kg/m^3); δ_p represents the cell thickness (m); c_p is the areal heat capacity of the PV cell, J/(m^2·K); G_p denotes the solar irradiance absorbed by the PV surface (W/m^2); Q_e represents the electrical power output of the PV cell; h_{c_abm} is the convective heat transfer coefficient between the PV surface and the ambient air (W/(m^2·K)), evaluated from the local wind speed [40]; h_{r_env} denotes environmentthe exterior radiative heat transfer coefficient; the radiative exchange follows the Stefan–Boltzmann law and is determined by the surface emissivity, in W/(m^2·K) [41], in which ε_p denotes the emissivity of the PV surface and σ is the Stefan–Boltzmann constant; k_p represents the thermal conductivity of the PV cell, W/(m·K).

$$h_{c_abm} = 6.5 + 3.3u_a \tag{2}$$

$$h_{r_\mathrm{env}} = \sigma\varepsilon_p\left(T_{amb} + T_p\right)\left(T_{amb}^2 + T_p^2\right) \tag{3}$$

The net radiative exchange between the pv cell module and the sky and surroundings consists of two contributions: the outward thermal emission from the pv cell, together with the downward atmospheric radiation received by the pv cell from the sky and environment. Subtracting the absorbed irradiation from the emitted radiation gives the net radiative heat loss, expressed by pv cell [34,42]:

$$Q_{r_net} = \varphi(Q_{r_p} - Q_{r_s}) \tag{4}$$

$$Q_{\mathrm{r_}p} = 2\int_0^\infty \int_0^{\pi/2} \varepsilon_{p,\lambda}(\lambda,\theta)\cdot E_{b,\lambda}(\lambda,T_p) sin\theta cos\theta d\theta d\lambda \tag{5}$$

$$Q_{\mathrm{r_s}} = 2\int_0^\infty \int_0^{\pi/2} \varepsilon_{s,\lambda}(\lambda,\theta)\cdot E_{b,\lambda}(\lambda,T_{amb})\cdot\alpha_{p,\lambda} sin\theta cos\theta d\theta d\lambda \tag{6}$$

where φ represents the inclination factor of the collector; $\varepsilon_{p,\lambda}$ denotes the spectral emissivity of the pv cell; $\varepsilon_{s,\lambda}$ represents the sky spectral emissivity; $\alpha_{p,\lambda}$ is the spectral absorptance of the pv cell; $E_{b,\lambda}$ stands for the spectral blackbody radiance at wavelength λ and temperature T, $\mathrm{W/(m^2 \cdot \mu m \cdot sr)}$, governed by Planck's law as $\varphi\varepsilon_{p,\lambda}\varepsilon_{s,\lambda}\alpha_{p,\lambda}E_{b,\lambda}\lambda T\mathrm{W/(m^2 \cdot \mu m \cdot sr)}$. For the present configuration the roof absorber is inclined at 30° to the horizontal and the wall module is vertical (90°), and these inclinations are the values used in the view-factor integrals of Equations (5) and (6).

$$E_{b,\lambda}(\lambda,T) = \frac{2\pi \mathrm{hc}^2}{\lambda^5}\frac{1}{e^{\frac{hc}{\lambda k_B T}} - 1} \tag{7}$$

where h denotes Planck's constant, J · s; c represents the speed of light in vacuum (m/s); k_B is the Boltzmann constant (J/K); and λ denotes the wavelength (m).

3.1.2. Heat-Balance Equation of Air in the Flow Channel of PV-TC Wall

The channel air exchanges convective heat with both the pv cell and the wall on its two sides, and the corresponding energy balance reads the heat balance equation can be expressed as follows:

$$\rho_{\mathrm{a}} c_a \delta_a \frac{\partial T_a}{\partial t} = h_{c_a,p}(T_p - T_a) + h_{c_a,w}(T_w - T_a) - \rho_{\mathrm{a}}\delta_a c_a V_a \frac{\partial T_a}{\partial x} \tag{8}$$

where $h_{c_a,w}$ denotes the convective heat transfer coefficient between wall and the channel air $\mathrm{(W/(m^2{\cdot}K))}$; $\mathrm{W/m^2{\cdot}K}$ and V_a represents the air velocity inside the channel (m/s).

For the naturally ventilated channel, the buoyancy-driven airflow rate is evaluated from

$$V_{\mathrm{a}} = \sqrt{\frac{g\beta(T_{out} - T_{in})H}{c_{in}(A/A_{in}) + c_{out}(A/A_{out}) + c_f(H/de)}} \tag{9}$$

where T_{out} and T_{in} denote the inlet and outlet air temperatures of the channel, respectively (°C); H is the channel height (m); A represents the channel cross-sectional area $(\mathrm{m^2})$; A_{in}, A_{out} correspond to the inlet and outlet opening areas, respectively $(\mathrm{m^2})$; de denotes the hydraulic diameter of the duct (m); C_f, C_{in}, C_{out} denote the channel friction factor and the inlet/outlet loss coefficients, respectively; $C_{in} = 1.0$, $C_{out} = 1.5$. The friction factor C_f is given by:

$$\mathrm{c}_f = 64/\mathrm{Re} \qquad \mathrm{Re} < 2000 \tag{10}$$

$$\mathrm{c}_f = 0.3164\mathrm{Re}^{-0.25} \qquad \mathrm{Re} > 4000 \tag{11}$$

Under forced convection, the channel air velocity is fixed at 0.2 m/s.

3.1.3. Heat-Balance Equation of PV-DH Roof

In the numerical model, T_p, T_{ma}, T_{tg} and T_{mof} denote the temperatures of the PV cell, moist airflow, thermal grease, and MOF layer, respectively.

The corresponding energy balance for the roof PV cell is written as:

$$\rho_p \delta_p c_p \frac{\partial T_p}{\partial t} = G_p - Q_e + h_{c_abm}\left(T_{amb} - T_p\right) + h_{r_sky}\left(T_{sky} - T_p\right) + \frac{k_p}{\delta_p}\left(T_{mof} - T_p\right) \quad (12)$$

where ρ_p denotes the density of the PV cell (kg/m^3); δ_p represents the cell thickness (m); c_p is the areal heat capacity of the PV cell, J/(m^2·K); G_p denotes the solar irradiance absorbed by the PV surface (W/m^2); Q_e represents the electrical power output of the PV cell; h_{c_abm} is the convective heat transfer coefficient between the PV and ambient air (W/(m^2·K)), evaluated from the local wind speed; T_{sky} denotes the effective sky temperature, which is inferred from the dry-bulb air temperature [35]; h_{r_sky} is the radiative heat transfer coefficient to the sky; this radiative exchange follows the Stefan–Boltzmann law and is determined by the surface emissivity (W/(m^2·K)), in which ε_p denotes the PV surface emissivity and σ is the Stefan–Boltzmann constant; k_p represents the thermal conductivity of the PV cell, W/(m·K).

$$T_{sky} = 0.0552 \times T_a^{1.5} \quad (13)$$

$$h_{c_abm} = 6.5 + 3.3u_a \quad (14)$$

$$h_{r_sky} = \sigma \varepsilon_p \left(T_{sky} + T_p\right)\left(T_{sky}^2 + T_p^2\right) \quad (15)$$

The energy balance for the roof airflow is expressed as:

$$\frac{1}{V_m}\frac{\partial T_{ma}}{\partial t} = \frac{4h}{d_e V_m \rho_{ma} c_{ma}}\left(T_{mof} - T_{ma}\right) - u_{\mathrm{m}}\frac{\partial T_{ma}}{\partial x} \quad (16)$$

where ρ_{ma} denotes the density of moist air (kg/m^3); c_{ma} represents the heat capacity of moist air, J/(kg·K); V_m is the mean airflow velocity (m/s); d_e denotes the equivalent hydraulic diameter (m); h is the convective heat transfer coefficient between the moist air and the MOF layer.

The heat balance for the MOF layer is given below:

$$\rho_d \delta_{mof} c_{tot} \frac{\partial T_{mof}}{\partial t} = q_{st}\rho_d \frac{\partial q}{\partial t} + h_{c_a,mof}\left(T_{ma} - T_{mof}\right) + \frac{k_{mof}}{\delta_{mof}}\left(T_p - T_{mof}\right) \quad (17)$$

where ρ_d denotes the density of the dry sorbent (kg/m^3); k_d represents the thermal conductivity of the dry sorbent (W/(m·K)); $h_{c_a,mof}$ denotes the convective heat transfer coefficient between the MOF layer and the channel air (W/(m^2·K)); w is the moisture content of the sorbent, kg/kg; q_{st} denotes the adsorption heat, J/kg; c_{tot} is the effective volumetric heat capacity of the MOF layer, J/(kg·K); δ_{mof} represents the MOF layer thickness (m); k_{mof} denotes the thermal conductivity of the MOF layer (W/(m·K)).

$$c_{tot} = c_{pd} + qc_{pw} \quad (18)$$

3.1.4. Mass-Balance Equation of Formaldehyde Degradation

The species balance couples two key quantities: the thermal-catalytic oxidation rate and the convective pollutant mass-transfer rate. Applying conservation over a differential control volume of the channel yields

$$W\delta_a \frac{\partial c(x,t)}{\partial t} dx = (QC(x,t) - Q(C(x,t) + \frac{\partial c(x,t)}{\partial t} dx)) - r_f W dx \quad (19)$$

where W denotes the reaction-surface width normal to the flow direction (m); δ_a represents the channel thickness (m); C is the mainstream formaldehyde concentration in the channel (ppb); Q denotes the volumetric airflow rate (m^3/s); r_f represents the catalytic-surface consumption rate, i.e., the amount of formaldehyde oxidized per unit catalyst area per second (ppb·m/s).

At the gas–catalyst interface, the steady-state mass balance equates the convective transport from the mainstream to the surface consumption, written as

$$m(x) = r_f(x) = h_m(x)(C(x) - C_s(x)) = k_{app}(x)C_s(x) \quad (20)$$

where m denotes the convective mass-transfer flux from the mainstream to the catalyst surface (ppb·m/s); C_s represents the formaldehyde concentration at the catalyst surface (ppb); k_{app} is the local apparent reaction-rate coefficient, which depends on the surface HCHO concentration, water-vapor concentration and catalyst temperature (m/s); h_m denotes the local convective mass-transfer coefficient (m/s).

h_m and C_s are evaluated from the following relations [43].

h_m and C_s for the nominal channel of 0.04 m gap, 3 m width and 0.2 m/s, the hydraulic diameter is 0.079 m and the Reynolds number is about 1.0×10^3, that is, laminar. With Sh ≈ 7.5 for fully developed flow between parallel plates at constant wall concentration, the convective mass-transfer coefficient is about 1.8×10^{-3} m/s and the corresponding single-pass conversion, $1 - \exp(-k_c\ a\ L/u)$, is about 0.8. This is the transport ceiling of the channel at the stated operating point: the conversions reported in Sections 4.1.1 and 4.1.2 approach it, and the values above it at the lowest inlet concentrations indicate that the one-dimensional plug-flow treatment with a mass-transfer resistance in series is optimistic in that range. A two-dimensional or CFD treatment of the catalytic channel has not been performed and is identified as necessary future work.

$$Sh = NuLe^{1/3} = \frac{h_m d_e}{D_{HCHO}} \quad (21)$$

$$C_s(x) = \frac{C(x)}{1 + k_{app}(x)/h_m(x)} \quad (22)$$

where D_{HCHO} denotes the molecular diffusion coefficient of HCHO in air (m^2/s);

Combining Equations (20)–(22) into Equation (19) gives:

$$\frac{\partial c(x)}{\partial t} + u_a \frac{\partial c(x)}{\partial x} + \frac{h_m(x)}{\delta_a}(C(x) - C_s(x)) = 0 \quad (23)$$

The widely used Langmuir–Hinshelwood-type kinetic expression for thermal catalytic oxidation is adopted below [44]:

$$r_f = kKe^{-\frac{E}{RT}} e^{-\frac{H}{RT}} C_s/(1 + Ke^{-\frac{H}{RT}} C_s) \quad (24)$$

here, the numerical values of the kinetic parameters are: $k = 5.62 \times 10^3$ m·ppb·s^{-1}, $K = 5.78 \times 10^{-5}$ ppb^{-1}. The apparent activation energy corresponds to an increase of only about 20% in the intrinsic rate between 10 and 50 °C.

Note: the numbers listed above are the actual numerical magnitudes of the kinetic parameters used in the present transient simulation, rather than symbolic definitions; they are adopted directly from our earlier experimentally validated α-MnO_2 catalytic model [44] and are held fixed throughout the subsequent parametric analysis.

The catalytic oxidation performance is influenced by both catalyst temperature and the moisture content of the air. The temperature-dependent kinetic term in Equation (24) describes the effect of catalyst temperature on the reaction rate. Within the applicable operating range, an increase in catalyst temperature generally promotes the oxidation reaction. In addition, water vapor may affect formaldehyde adsorption and surface reaction processes by competing for adsorption sites or modifying the surface hydroxylation state of the catalyst. However, the magnitude and direction of the humidity effect depend on the catalyst composition and operating temperature. For example, Pei et al. [39] reported a significant influence of relative humidity on formaldehyde oxidation over a CuO/MnO_2 catalyst, particularly at relatively low temperatures. Since the catalyst composition differs from the α-MnO_2 catalyst considered in this study, these findings are used only to illustrate the potential influence of humidity and should not be directly interpreted as the quantitative humidity dependence of α-MnO_2. The present study does not provide an independent quantitative sensitivity analysis of relative humidity for the α-MnO_2 catalytic layer. The kinetic coefficients of the formaldehyde oxidation reaction used here, namely the reaction rate constant, the adsorption equilibrium constant, the activation energy and the reaction enthalpy appearing in Eq. (24), together with the reference photovoltaic efficiency and its temperature coefficient, are those of the previously validated models reported in our earlier work [44].

3.1.5. Mass-Balance Equation

The species balance for the channel airflow is written as:

$$\frac{1}{V_m}\frac{\partial(d_{ma})}{\partial t} = \frac{4h_m}{d_e u_m}\left(d_{mof} - d_{ma}\right) - u_{\mathrm{m}}\frac{\partial d_{ma}}{\partial x} \tag{25}$$

where d_{mof} denotes the MOF moisture content (g/kg); h_m represents the convective mass-transfer coefficient between moist air and the MOF layer; $Le^{2/3}$ is the Lewis number.

$$h_m = \frac{h}{\rho_{ma} c_{ma} Le^{2/3}} \tag{26}$$

The change in airflow humidity driven by MOF adsorption is described by

$$P_{\mathrm{v},out} = \frac{P\omega_{out}}{0.62198 + \omega_{out}} \tag{27}$$

here, P denotes the total atmospheric pressure, (Pa); ω_{out} represents the outlet air humidity ratio (kg water/kg dry air), and $p_{v,out}$ is the outlet water-vapor partial pressure (Pa).

The saturation vapor pressure, which sets the upper bound of water-vapor concentration at a given temperature, is evaluated from.

The uptake q used in Equation (31) is expressed per unit mass of dry sorbent, whereas the channel air is described by its humidity ratio; the two quantities are related through the ratio of the sorbent mass to the dry-air mass flow, d_{mof}/d_a, which is evaluated from the coated sorbent mass and the instantaneous airflow rate. The vapor-pressure driving force and the uptake are therefore computed on a consistent mass basis, and no separate conversion factor is applied to the isotherm.

$$P_{sat} = 611 \cdot exp\left(\frac{17.27 \cdot \left(T_{a,out} - 273.15\right)}{T_{a,out} - 35.85}\right) \tag{28}$$

This empirical correlation expresses the temperature dependence of the saturation vapor pressure, in which P_{sat} denotes the saturation vapor pressure (Pa). As expected, p_sat rises monotonically with temperature.

Once the relative humidity is known, the actual water-vapor partial pressure is obtained by scaling p_sat:

$$RH_{out} = \frac{P_{v,out}}{P_{sat}} \times 100\% \tag{29}$$

The equilibrium MOF uptake q as a function of water-vapor pressure is described by the Langmuir isotherm [45]:

$$q_{eq} = q_{max} \cdot \frac{K_{MOF} \cdot P_{v,out}}{1 + K_{MOF} \cdot P_{v,out}} \tag{30}$$

here, q_{max} denotes the saturation uptake of the MOF (kg/kg); K_{MOF} is the adsorption equilibrium constant (1/kPa). The isotherm predicts that uptake grows with vapor pressure before plateauing at q_max. It should be noted that water uptake in MIL-101(Cr) follows an S-shaped, type V isotherm, and that a single-site Langmuir form cannot reproduce the step that occurs at intermediate relative pressure or the temperature dependence of the equilibrium constant. The formulation used here is therefore appropriate for interpolating within the operating range examined in this study, but not for predicting uptake across the full humidity range; a temperature-dependent characteristic-curve or Dubinin–Astakhov description would be required for that purpose.

Because the equilibrium uptake in this formulation is fixed by the vapor pressure computed from the outlet air relative humidity and temperature, it does not contain the sorbent temperature as an independent variable; the additional uptake produced by radiatively cooling the sorbent at a fixed air state is therefore not represented, and the night-time benefit of radiative cooling in the present model arises only through the reduction in the air temperature.

The transient adsorption rate dq is governed by the linear driving-force expression, where k_{LDF} denotes the rate constant and $q_{eq} - q$ is the uptake driving force, written as [40]:

$$\frac{dq}{dt} = k_{LDF}\left(q_{eq} - q\right) \tag{31}$$

here, k_{LDF} denotes the LDF rate constant (1/s); q_{eq} represents the equilibrium uptake (kg/kg); q is the instantaneous uptake (kg/kg), and d_t is the simulation time step (s). This first-order relaxation relation drives q toward q_eq over successive time steps. The equilibrium used for the reported results is the Langmuir relation above, with vapor pressure in kPa, q_max = 1.2 kg/kg, K_iso = 0.5 kPa^{-1}, and k_LDF = 0.0003 s^{-1}. It does not reproduce the S-shaped isotherm of MIL-101(Cr), and it was not replaced by another isotherm. K_iso is constant. Temperature changes the calculated uptake because the vapor pressure is obtained from the relative humidity and the saturation pressure.

Because q_max and k_LDF are held constant, the equilibrium capacity of the layer scales linearly with its thickness and the internal diffusion and conduction resistances are omitted. In addition, the Langmuir constant K_iso = 0.5 kPa^{-1} gives an appreciable uptake at low relative humidity, whereas the measured isotherm of MIL-101(Cr) is close to zero in that range, so the low-humidity end of the operating envelope is overpredicted.

3.1.6. Optimization Algorithm

The PV-TC/DH hybrid system involves multiple coupled functions, including photovoltaic electricity generation, air purification, and dehumidification. Due to the interaction among different design parameters and performance indicators, improving one objective may result in a reduction in other objectives. Therefore, a multi-objective optimization framework was established to determine the optimal configuration of the proposed system [46,47]. The optimization problem was formulated based on the developed transient heat and mass transfer model. Six design variables that significantly affect the system

performance were selected as optimization variables, including the wall air gap thickness, roof air gap thickness, MOF layer thickness, night-time airflow rate, wall PV coverage ratio, and roof PV coverage ratio.

The corresponding lower and upper boundaries of the optimization variables were determined according to the feasible design ranges of the PV-TC/DH system, as summarized in Table 2. The wall and roof air gaps were constrained within 0.015–0.040 m and 0.030–0.080 m, respectively. The MOF thickness was varied from 0.001 to 0.006 m, while the night-time airflow rate ranged from 0.006 to 0.024 m^3/s. The PV coverage ratios of both wall and roof modules were limited between 0.2 and 0.9. These ranges were chosen from manufacturable and structurally feasible values. As shown in Section 4.3.1, several of the selected optima lie on these bounds, which indicates that the corresponding variables are constrained by the prescribed interval rather than by an internal trade-off; the intervals should therefore be widened in future optimizations before the resulting trends are interpreted physically.

Table 2. The value range of the optimization variables.

Variable	Symbol	Range	Unit
Wall air gap	d_{wall}	0.015–0.040	m
Roof air gap	d_{roof}	0.030–0.080	m
MOF thickness	d_{MOF}	0.001–0.006	m
Night airflow rate	V	0.006–0.024	m^3/s
Wall PV coverage	$C_{PV,w}$	0.2–0.9	-
Roof PV coverage	$C_{PV,r}$	0.2–0.9	-

The Non-dominated Sorting Genetic Algorithm II (NSGA-II) was employed to solve the multi-objective optimization problem. NSGA-II is an evolutionary algorithm that identifies optimal solutions based on Pareto dominance, while maintaining population diversity through crowding distance evaluation. In each iteration, candidate solutions were generated through selection, crossover, and mutation operations, and their objective values were calculated by coupling the optimization algorithm with the developed PV-TC/DH simulation model. The calculation flow chart after coupling the optimization algorithm and the established mathematical model is shown in Figure 4. In this study, the population size was set to 40 and the maximum iteration number was set to 15. The crossover probability and mutation probability were 0.8 and 0.2, respectively. During each optimization cycle, the generated solutions were evaluated according to the three objective functions, followed by non-dominated sorting and population updating until convergence. The final optimization results consisted of a set of Pareto-optimal solutions representing different trade-offs among electricity generation, clean air production, and dehumidification performance. To determine the most suitable compromise solution, the Technique for Order Preference by Similarity to Ideal Solution (TOPSIS) method was subsequently applied to select the final optimal configuration. These settings were chosen to keep the computational cost of each optimization run tractable, since every candidate solution requires a complete dynamic simulation of the system. The population size and the number of generations are therefore modest, and a formal convergence study, for example the evolution of the hypervolume or repeated runs with different random seeds, has not been carried out. The Pareto fronts presented in Section 4.3.1 should accordingly be regarded as representative rather than fully converged, and the configurations selected from them as near-optimal designs.

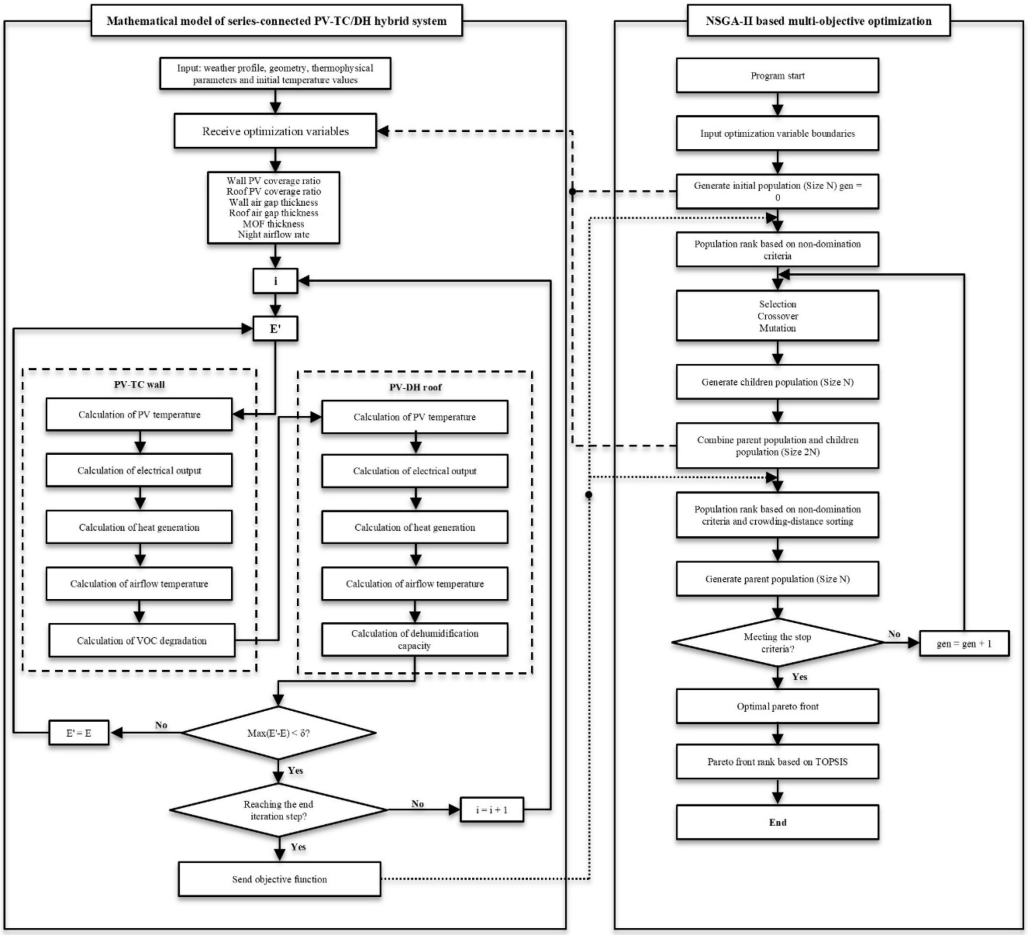


Figure 4. The flow chart of the calculation process.

3.2. Evaluation and Validation

3.2.1. Performance Evaluation Indexes

Depending on the operating mode, the system simultaneously harvests solar heat, releases radiative cooling to the sky, and produces clean air. Accordingly, the evaluation indicators cover three aspects: heat gain, radiative cooling gain, and air-cleaning efficiency.

For heat gain:

$$Q_{\text{th}} = cm(T_{out} - T_{in}) \tag{32}$$

For radiative cooling gain:

$$Q_{\text{rc}} = cm(T_{in} - T_{out}) \tag{33}$$

where denotes the specific heat of air (J/(kg·K)); cJ/kg · K m represents the air mass (kg); T_{in} and T_{out} are the inlet and outlet air temperatures of the channel, respectively (°C).

Air-cleaning performance is quantified by the single-pass formaldehyde conversion and the *CADR*. They are computed as [18]:

$$\varepsilon = \frac{c_{\text{in}} - c_{out}}{c_{\text{in}}} \tag{34}$$

$$CADR = Q_{\varepsilon} = Q(1 - \frac{c_{out}}{c_{\text{in}}}) \tag{35}$$

where C_{in} and C_{out} denote the inlet and outlet formaldehyde concentrations of the channel, respectively (ppb); *CADR* represents the clean-air delivery rate, i.e., the equivalent clean-air volume supplied per unit time (m^3/h).

Over a full day, the total degraded HCHO mass and total clean-air volume are obtained by time-integrating *CADR*.

$$V_{\text{total}} = \int_0^{\tau} CADR dt \tag{36}$$

The single-pass conversion ratio and clean air delivery rate (CADR) characterize the formaldehyde-removal efficiency and the equivalent clean-air treatment capacity of the catalytic airflow channel, respectively. These indicators should be interpreted as measures of the treatment performance of the catalytic unit under the specified inlet condition. They do not directly represent the time-dependent room-average formaldehyde concentration or the cumulative exposure of occupants. A quantitative prediction of indoor pollutant concentration and exposure reduction requires a room-level pollutant mass balance that accounts for indoor formaldehyde emission sources, outdoor pollutant concentration, ventilation and infiltration rates, and pollutant transport within the room. Such a separate room-level exposure assessment is beyond the scope of the present study.

To further quantify the energy-saving benefit, the reduction in fresh-air conditioning load is estimated by comparing the cooling/heating demand of the intake air before and after the PV-TC/DH hybrid system. The corresponding load expression is:

$$Q_{cooling/heating} = cm(T_{room} - T_{amb}) \tag{37}$$

$$\text{Reduction } Ratio = \frac{Q_{cooling/heating,before} - Q_{cooling/heating,after}}{Q_{cooling/heating,before}} \times 100\% \tag{38}$$

where $Q_{cooling/heating}$ denotes the fresh-air cooling/heating load (J); m represents the air mass (kg).

The instantaneous electrical yield of the PV modules is evaluated from

$$E_{pv} = G\zeta\eta_{ref}\left[1 - B_r(T_{pv} - T_{ref})\right] \tag{39}$$

where E_{pv} denotes the PV electrical power output per unit area ($W \cdot m^{-2}$), η_{ref} is the nominal PV efficiency, $\eta_{ref} = 0.18$, and ζ is a correction factor taken into account for factors such as obstruction, B_r is the temperature coefficient of efficiency.

3.2.2. Multi-Criteria Decision Strategy

The NSGA-II algorithm can provide a group of Pareto-optimal solutions by balancing photovoltaic generation, clean air production, and dehumidification performance. However, since these solutions represent different trade-offs among multiple objectives, a further decision-making method is required to determine the most suitable configuration for practical application. Therefore, the TOPSIS method was adopted to identify the final compromise solution from the Pareto-optimal solution set.

The TOPSIS method evaluates each candidate solution according to its relative distance from the positive ideal solution and negative ideal solution. The positive ideal solution represents the best achievable performance among all Pareto solutions, while the negative ideal solution represents the worst performance. The optimal compromise solution is considered to be the one closest to the positive ideal solution and farthest from the negative ideal solution.

Since the objectives differ in dimension and scale, the raw decision matrix is normalized by [48]:

$$r_{ij} = \frac{y_{ij}}{\sqrt{\sum_{i=1}^{n} y_{ij}^2}} \tag{40}$$

After normalization, equal importance was assigned to the three objectives because the proposed PV-TC/DH hybrid system aims to achieve a balanced improvement in energy

generation and indoor environmental regulation. Therefore, the weighting coefficients were defined as:

$$w_1 = w_2 = w_3 = \frac{1}{3} \tag{41}$$

The weighted normalized matrix was obtained as:

$$v_{ij} = w_j r_{ij} \tag{42}$$

The positive and negative ideal solutions were then determined:

$$A^+ = \{v_1^+, v_2^+, v_3^+\} \tag{43}$$

$$A^- = \{v_1^-, v_2^-, v_3^-\} \tag{44}$$

where A^+ and A^- denote the best and worst values of each objective across the Pareto front, respectively.

The Euclidean distances between each candidate solution and the ideal solutions were calculated:

$$D_i^+ = \sqrt{\sum_{j=1}^{3} (v_{ij} - v_j^+)^2} \tag{45}$$

$$D_i^- = \sqrt{\sum_{j=1}^{3} (v_{ij} - v_j^-)^2} \tag{46}$$

The relative closeness coefficient was finally obtained:

$$C_i = \frac{D_i^-}{D_i^+ + D_i^-} \tag{47}$$

A higher value of C_i corresponds to better overall performance across all objectives. The Pareto point with the largest closeness coefficient is therefore adopted as the final optimal compromise design.

In addition, the optimized configuration was compared with the baseline design to quantify the improvement achieved by multi-objective optimization. The baseline case was defined according to the original system parameters, and the performance differences between the optimized and baseline configurations were evaluated in terms of electricity generation, clean air production, and dehumidification capacity.

3.3. Method of Solution

To evaluate the comprehensive annual performance of the proposed building-integrated hybrid system across its core functions of heating, cooling, air purification, and dehumidification, a dedicated numerical simulation code was developed in MATLAB based on the aforementioned coupled heat and mass transfer model. The numerical discretization of the coupled heat and mass transfer equations at each computational node was implemented using a fully implicit finite difference method. Key meteorological input parameters, including outdoor air dry-bulb temperature, global horizontal solar irradiance, and ambient wind speed, were extracted from the Typical Meteorological Year (TMY) dataset bundled with Energy Plus. Previous studies of thermal-catalytic purification walls adopted an inlet formaldehyde concentration of 600 ppb [21,24]; the same value is used here, and it represents an elevated-pollution benchmark [4,5] condition rather than the typical background concentration in normally occupied residential environments. All pollutant-removal results presented in this study are based on this fixed baseline concentration. The effects of lower and time-varying inlet formaldehyde concentrations are not independently evaluated in the present work. The detailed computational parameters used in the model are shown in Table 3. An inlet concentration of 600 ppb corresponds to approximately 0.74 mg/m^3

at room temperature and pressure, which is well above the guideline values commonly adopted for residential indoor air, and the purification results should be read in that light. The irradiance incident on the inclined roof and on the vertical wall was obtained from the global horizontal irradiance of the weather file without decomposing it into beam, diffuse and ground-reflected components, and the sky temperature was evaluated with a clear-sky correlation that does not represent the effect of humidity or cloud cover; the radiative cooling potential under humid or overcast conditions is therefore likely to be overestimated. Condensation of water vapor on the radiatively cooled surfaces is likewise not represented.

Table 3. Detail computational parameters for the PV-TC/DH system.

	Symbol	Explanation	Units	Value
Room	Lr	Length	m	4
	Wr	Width	m	3.8
	Hr	Height	m	3
PV panel (wall and roof)	λ_p	Thermal conductivity	$(m^2 \cdot K)W/(m{\cdot}K)$	1.5
	c_p	Specific heat capacity	$J/kg \cdot KJ/(kg{\cdot}K)$	750
	p_p	Density	kg/m^3	2350
	δ_p	Thickness	m	0.003
	α_p	Absorptivity	-	0.92
	ε_p	Emissivity	-	0.88
	Lp	Length	m	4 (wall)/4 (roof)
	Wp	Width	m	3
Airflow channel	δ_{ac}	Thickness	m	0.04
	Lac	Length	m	4
	Wac	Width	m	3
Air	λ_a	Thermal conductivity	$(m^2 \cdot K)W/(m{\cdot}K)$	0.026
	c_a	Specific heat capacity	$J/kg \cdot KJ/(kg{\cdot}K)$	1005
	p_a	Density	kg/m^3	1.18
	μ_a	Kinematic viscosity	$N \cdot s/m^2m^2/s$	1.58×10^{-5}
	V_a	Flow velocity	m/s	0.2
Vent	A	Area	m^2	0.45
Wall	λ_w	Thermal conductivity	$(m^2 \cdot K)W/(m{\cdot}K)$	1.5
	c_w	Specific heat capacity	$J/kg \cdot KJ/(kg{\cdot}K)$	970
	p_w	Density	kg/m^3	2000
	δ_w	Thickness	m	0.2
	α_w	Absorptivity	-	0.2
	ε_w	Emissivity	-	0.8
Roof	λ_{roof}	Thermal conductivity	$(m^2 \cdot K)W/(m{\cdot}K)$	1.5
	c_{roof}	Specific heat capacity	$J/kg \cdot KJ/(kg{\cdot}K)$	970
	p_{roof}	Density	kg/m^3	2000
	δ_{roof}	Thickness	m	0.2
	ε_{roof}	Emissivity	-	0.8
Formaldehyde	C	Concentration	ppb	600
	D	Diffusion coefficient	m^2/s	1.86×10^{-5}
Constants	σ	Stefan–Boltzmann constant	$W/(m^2{\cdot}K^4)$	5.67×10^{-8}
	g	Gravitational acceleration	m/s^2	9.81
	R_v	Water vapor gas constant	$J/kg \cdot KJ/(kg{\cdot}K)$	461.5

3.4. Model Validation

In this work, model validation was performed individually on two key components: the PV-TC wall and the PV-DH roof. Uncertainty analysis was conducted using the root-mean-

square deviation (RMSD), and the corresponding results were systematically summarized and consolidated [35]. The RMSD serves as a quantitative metric for evaluating the discrepancy between model predictions and experimental measurements. Computation of this metric allowed us to assess the predictive accuracy of the model and to quantify the uncertainties associated with the simulation procedure. Based on these results, the error magnitude of the developed model was further evaluated using RMSD.As presented in Table 4, the maximum RMSD across all parameters remains below 8%, demonstrating that the overall error of the model is relatively small. The validation reported here refers to the two modules individually and does not constitute a validation of the series-connected system; the coupled configuration, the winter operating modes, and repeated adsorption–desorption cycling were not tested experimentally, and the system-level results in Section 4 are consequently model predictions obtained with component-validated sub-models. The deviations in Table 4 are defined as the root-mean-square of the differences between simulated and measured values, normalized point by point by the corresponding measured value, as in Equation (48). Because such a relative index depends on the absolute level of the measured quantity, and because relative humidity is bounded and referenced to saturation, these values are used here as an indication of agreement rather than as a formal error metric. Absolute RMSE, CV(RMSE) and NMBE computed over the complete measurement series, together with a propagation of the individual sensor uncertainties into the reported deviations, have not been derived and are identified as a limitation. For the same reason, the dehumidification performance is not validated through the humidity ratio and mass flow or gravimetrically, and the validation of the formaldehyde model refers to the conditions of the earlier experiments quoted in the text rather than to an independent data set.

Table 4. RMSD comparison of each parameter of the system.

Parameter	Outlet Air Temperature	PV Temperature	Power Density	Outlet Formaldehyde Concentration	Outlet Relative Humidity
RMSD	3.23%	2.71%	6.16%	4.57%	7.94%

The apparatus, instrumentation and measurement procedure of the two component experiments are those reported in [25,44] for the PV-TC wall and in [33] for the roof module, and they are not reproduced here.

$$RMSD = \sqrt{\sum \left[(x_{sti} - x_{exp}) / x_{exp} \right]^2 / n} \quad (48)$$

Figure 5 shows the relationship between the simulated values and experimental values to evaluate the predictive accuracy of the model. The data lines represent the experimental and simulated values for different performance metrics, indicating a strong consistency between the simulated and experimental results, thus validating the effectiveness of the model. Furthermore, the validation of the formaldehyde degradation model is based on our team's previous research on the PV-TC wall system. In this study, the goodness of fit between the model predictions and experimental data is as high as 0.94, demonstrating that this mass transfer model can accurately describe the catalytic degradation of formaldehyde within the flow channel [44]. And the roof solar photovoltaic thermal collection model and radiative cooling effect model employed in this study have been validated in earlier work, both exhibiting high predictive accuracy [25,36,37,49].

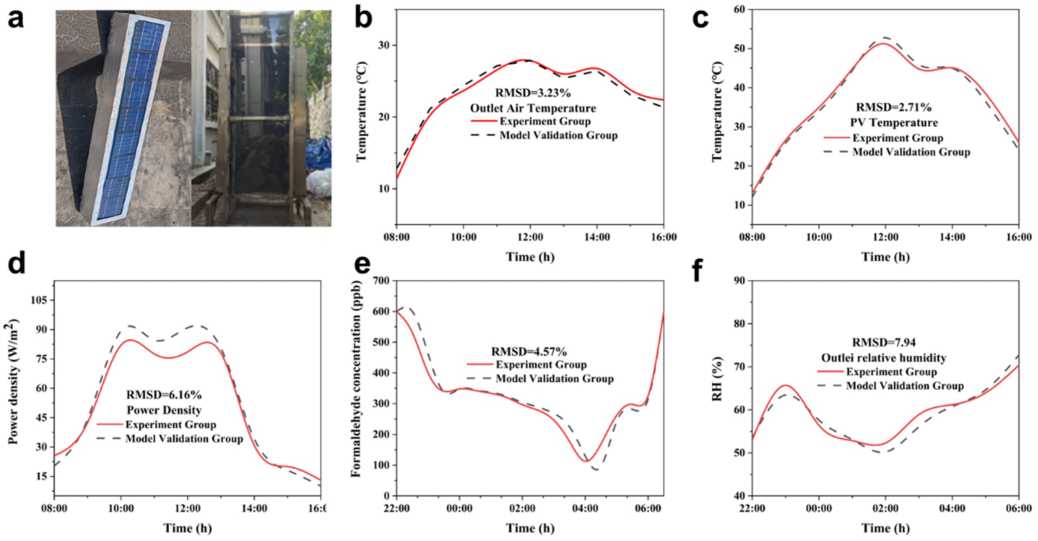


Figure 5. Model validation of the PV-TC/DH system: (**a**) schematic diagram of the experimental apparatus; (**b**) outlet air temperature (°C); (**c**) photovoltaic surface temperature (°C); (**d**) power density (W·m^{-2}); (**e**) outlet formaldehyde concentration (ppb); (**f**) outlet relative humidity (%). Simulated and measured values are plotted against time in each panel, and the panels correspond to the component-level experiments described in Section 3.4.

3.5. Research Case

To investigate the operational performance and energy-saving potential of the proposed hybrid system, a typical residential building room in Nanjing, China was selected as the test bed for a comprehensive case study. The test room has the following dimensions: 4 m (length) × 3.8 m (width) × 3 m (height), with an exterior wall thickness of 0.2 m. The exterior walls are represented as a 0.2 m homogeneous concrete layer with the properties listed in Table 3 (λ = 1.5 W/(m·K), ρ = 2000 kg/m^3, c_p = 970 J/(kg·K)); these are values for dense concrete rather than for aerated concrete, so the wall is more conductive and more massive than an aerated-concrete wall of the same thickness. The roof of the test room, measuring 4 m × 3 m, is constructed from reinforced concrete tiles to ensure long-term durability and structural stability. Figure 6a presents a three-dimensional schematic diagram of the test room, where the roof and south-facing exterior walls are integrated with PV panels and the corresponding photovoltaic thermal coating layers. The total active coverage area is 24 m^2, and the system delivers conditioned air (heated or cooled) to the indoor space on demand. Furthermore, annual meteorological data for Nanjing were retrieved from the official Energy Plus weather data repository. Figure 6b presents the monthly mean, maximum, and minimum ambient air temperatures for Nanjing. The indoor air temperature is treated as a prescribed boundary condition rather than as a simulated variable: no room-level heat and moisture balance is solved, and the cooling and heating outputs reported in Section 4 therefore quantify the effect of the envelope and of the supply air rather than the resulting indoor operative temperature or relative humidity. The fresh-air rate of the reference case, used when the reduction in fresh-air load is evaluated, is that associated with the simulated supply airflow. A whole-building simulation, for example a coupling to EnergyPlus for the zone heat and moisture balance in addition to the weather data, has not been performed.

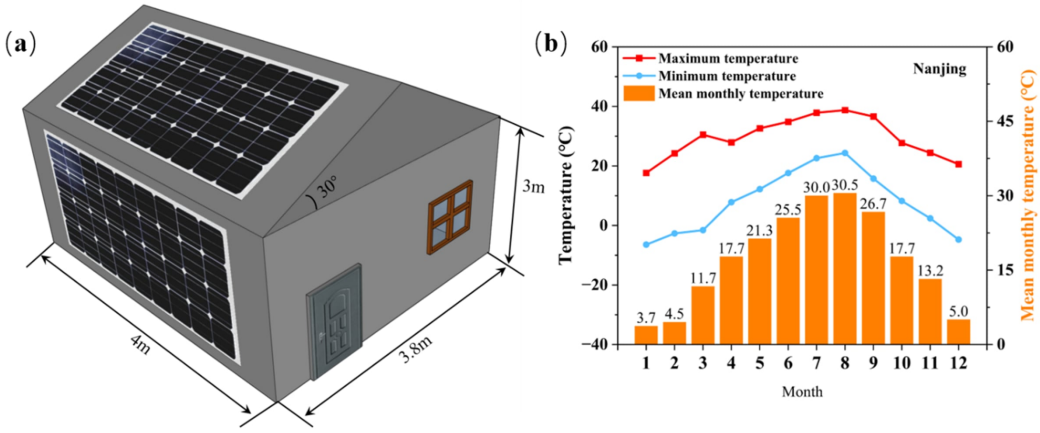


Figure 6. (**a**) The 3D visualization of the building room. (**b**) The annual weather conditions of Nanjing.

4. Results and Discussions

To assess the comprehensive performance of the proposed hybrid system across its core functions of solar thermal collection, radiative cooling, photovoltaic thermal formaldehyde degradation, dehumidification, and photovoltaic power generation, a detailed case study was conducted for Nanjing, China. Key performance parameters, including PV panel temperature, PV power output, dehumidification capacity, outlet formaldehyde concentration, formaldehyde single-pass conversion efficiency, and clean air delivery rate (CADR), were numerically simulated and quantified across summer, winter, and transition seasons. These granular performance analyses provide quantitative insights into the system's operational effectiveness under distinct seasonal climatic conditions. Additionally, to investigate the system's performance across diverse climatic regions, Beijing, Shenzhen, and Xining were selected as representative locations for cross-comparative analysis. The annual solar thermal collection gain, annual radiative cooling capacity, cumulative clean air delivery, annual total dehumidification capacity, and annual net PV power generation of the system in these four cities were systematically calculated and cross-compared. The comparison across the four zones is reported as a set of model outputs for the meteorological years adopted: it shows where the configuration performs well, but it does not by itself establish geographical adaptability.

4.1. Performance Analysis of the System in Different Seasons

4.1.1. Performance Analysis in Summer

July was chosen as the representative month to assess the summer performance of the system. Figure 7a compares the variations in air temperature at the inlet and outlet of the flow channel between the proposed integrated system and the single PV-DH roof system over two consecutive days (15–16 July). The results demonstrate that the outlet air temperature of the proposed system is 4–6 °C higher than that of the single PV-DH roof system during daylight hours. This is attributed to the fact that outdoor air first enters the PV-TC wall, is preheated by solar energy, and subsequently flows into the flow channel of the PV-DH roof. This preheating process enhances the synergistic thermal effect between photovoltaic waste heat and solar radiation, significantly accelerating the desorption and regeneration of moisture within the MOF adsorption layer, thereby reserving a greater capacity for night-time dehumidification. During night-time, the outlet temperature of the proposed system is 3–4 °C lower than that of the single PV-DH roof system, which is due to the fact that air is initially cooled by radiative cooling in the PV-TC wall and subsequently further cooled in the PV-DH roof, thereby enhancing the night-time dehumidification potential of

the entire system. Quantitative calculations indicate that the summer cooling capacity of the proposed system is increased by 79.2% compared with the single PV-DH roof system. Accordingly, Figure 7b illustrates the variations in air humidity at the inlet and outlet of the flow channel for the two systems. When the system operates in outdoor circulation mode during daylight hours, the outlet humidity of the proposed system is significantly higher than that of the single PV-DH roof system, indicating a stronger desorption and regeneration capacity. When operating in indoor circulation mode during night-time, the outlet humidity of the proposed system is significantly lower than that of the single PV-DH roof system, demonstrating superior dehumidification performance. When the outlet humidity is lower than the inlet humidity, the system is engaged in dehumidification and air purification processes. Conversely, when the outlet humidity is higher than the inlet humidity, the system is in the MOF regeneration phase. Overall, the dehumidification capacity of the proposed system is enhanced by 26.9% relative to the single PV-DH roof system. Figure 7c depicts the variation trends of photovoltaic power generation density and ambient irradiance over a two-day period, indicating that the proposed hybrid system exhibits efficient solar energy utilization and stable power output capabilities. Figure 7d illustrates the temporal variations in the formaldehyde concentration at the outlet of the catalytic airflow channel and the corresponding single-pass conversion ratio. As indoor formaldehyde-containing air passes through the PV-TC wall, formaldehyde is decomposed over the α-MnO_2 catalytic layer, resulting in a reduction in the formaldehyde concentration of the treated airflow. The outlet concentration and single-pass conversion ratio therefore characterize the pollutant-removal performance within the catalytic channel under the specified inlet condition. The corresponding clean air delivery rate further indicates the treatment capacity of the system. These channel-level results should not be directly interpreted as the time-dependent average formaldehyde concentration in the entire room.

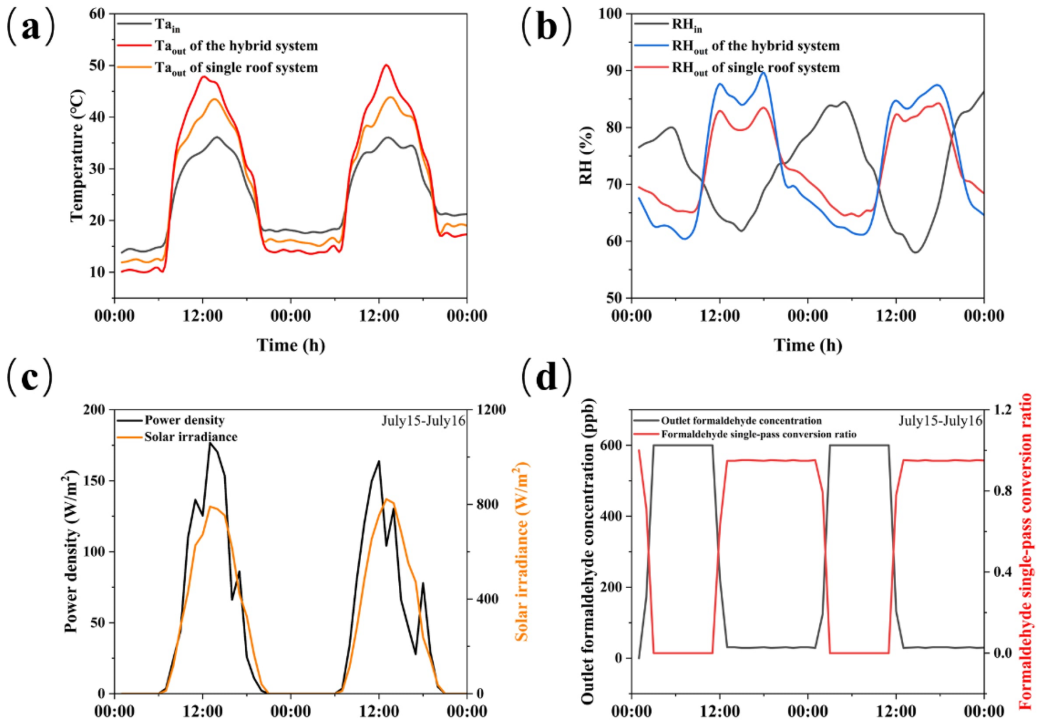


Figure 7. System performance in July 15 to July 16: (**a**) Variation in air temperature at the inlet and outlet of the airflow channel. (**b**) Variation in air humidity at the inlet and outlet of the airflow channel. (**c**) Variation in photovoltaic panel power generation density. (**d**) Variation in outlet formaldehyde concentration and single-cycle formaldehyde conversion ratio.

It should be noted that the catalytic activity at 10–25 °C is not equivalent to that at 40–60 °C, and that the temperature dependence of the fitted kinetics is weak: with the activation energy given above, the intrinsic rate increases by only about 20% between 10 and 50 °C. The photovoltaic heat nevertheless acts on the system in two ways, raising the operating temperature of the α-MnO_2 layer and supplying the low-grade heat that preheats the airflow and drives regeneration of the downstream MOF; because the catalyst is active at low temperature in its own right, the 40–60 °C heat contributes mainly to the regeneration duty, while the corresponding gain in catalytic rate is modest. Measurements on MnO_2-based catalysts at indoor concentrations support low-temperature operation: a single pass at room temperature removed about 92% of 0.5 mg/m^3 (≈400 ppb) and about 89% of 1.0 mg/m^3 (≈800 ppb) of formaldehyde at a space velocity of 600 L/(g_cat·h), and the activity was little affected by relative humidity between 4% and 80% [50]; in a static test at about 1 ppm and a relative humidity of 55%, a surface-modified MnO_2 removed the formaldehyde completely within 3 h, against about 37% over the unmodified oxide [51]. These measurements refer to MnO_2-based catalysts rather than to the α-MnO_2 coating used here; the rate expression employed in the model is taken from [44], and the competing adsorption of water vapor is not resolved by the kinetic model. However, it is acknowledged that the presence of high relative humidity at night introduces competitive adsorption between water vapor and formaldehyde on the active sites. Although our previous experimental tests confirmed that the α-MnO_2 surface retains sufficient catalytic activity under humid conditions, the kinetic model employed in this study (Equation (24)) simplifies this effect and does not fully decouple the dynamic water-vapor competition. Furthermore, this study assumes complete mineralization of formaldehyde to CO_2 and H_2O. The generation of intermediate by-products (such as CO and formic acid), the long-term deactivation of the catalyst, and the potential physical adsorption of unreacted formaldehyde or VOCs onto the downstream MIL-101(Cr) MOF layer were not explicitly quantified in the current transient model. The MOF layer may act as a secondary adsorption barrier for residual VOCs, but this specific interaction requires further dedicated experimental investigation. Future work will focus on quantifying these by-products, evaluating the long-term stability of the catalytic layer, and elucidating the coupled VOC-water adsorption mechanisms on the MOF.

We further analyzed the performance of the system throughout the entire month of July. Figure 8a presents the ambient temperature and solar irradiance in Nanjing for July, indicating that ambient temperatures fluctuate between 22.6 °C and 37.9 °C, with a peak solar irradiance of approximately 950 W/m^2. The PV panels absorb solar heat during the day and emit radiant energy for cooling at night. The PV panel temperature reached a peak of 70.3 °C on 14 July, as shown in Figure 8b. This elevated temperature highlights the system's capability for solar thermal collection during peak sunlight hours. In the simulation the mode is set by the schedule of Section 2.2, that is, external circulation during the daytime window and internal circulation for the remaining hours. In this mode, radiative cooling lowers the temperature of the PV surface and of the supply air, and the lowered air temperature increases the equilibrium uptake of the MOF layer, while the catalytic layer continues to oxidize formaldehyde in the air passing through the channel. These are outputs of the envelope model: no room-level balance is solved, so the extent to which the room air temperature, the room-average formaldehyde concentration or the indoor humidity would be modified in an occupied room is not established here. Conversely, during daytime, the system switches to the external circulation mode. Throughout July, the model alternates between the two circulation configurations and predicts cooling, dehumidification and purification of the air passing through the channel, together with electrical output; the corresponding indoor-air-quality and humidity benefits cannot be quantified without a

room model, and the percentages in Section 4.1 are configuration-level rather than area-normalized indicators. The maximum daily radiative cooling gain reached 3287 Wh, the maximum daily dehumidification capacity reached 3.68 L, the peak photovoltaic power generation density reached 177.8 W/m^2, and the maximum daily purified air volume reached 1042.1 m^3, as shown in Figure 8c–f.

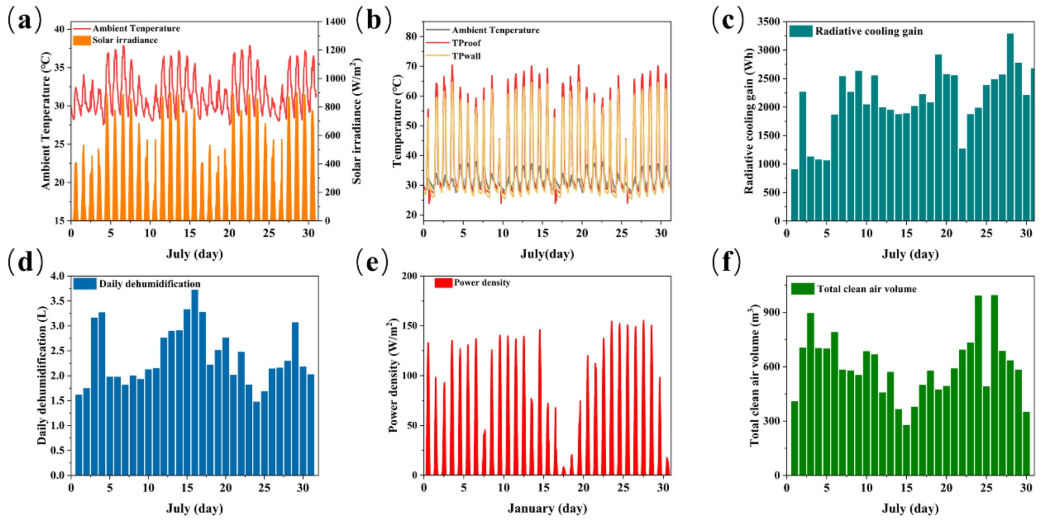


Figure 8. System performance in summer: (**a**) Meteorological parameters in Nanjing in July. (**b**) Comparison of photovoltaic temperature and ambient temperature. (**c**) Daily cooling capacity in July. (**d**) Daily dehumidification capacity in July. (**e**) Daily power generation in July. (**f**) Daily clean air production in July.

In summary, the simulation results indicate that the building-integrated photovoltaic thermal catalytic–dehumidification system can combine photovoltaic conversion, radiative cooling, thermal catalytic purification, and adsorption dehumidification within a single envelope, and that under the summer operating sequence considered the model predicts simultaneous electricity generation, cooling, humidity regulation, and formaldehyde removal. These results are model predictions for the specified operating sequence; they do not establish that acceptable indoor conditions are maintained in an occupied room, and the formaldehyde figures describe the treatment performance of the catalytic channel rather than the room-average concentration. In addition, the comparison in Figure 7 is made between configurations whose collector areas and airflow rates differ, so the percentage improvements quoted above are configuration-level indicators rather than area-normalized ones.

4.1.2. Performance Analysis in Winter

January was selected as the representative month for assessing the winter performance of the system. Figure 9a compares the variations in air temperature at the inlet and outlet of the flow channel between the proposed integrated system and the single PV-TC wall system over two consecutive days (15–16 January). The results demonstrate that the proposed integrated system delivers a continuous supply of heated air throughout the diurnal cycle in winter through the coordination of the PV-TC wall and the PV-DH roof. During daylight hours, the PV-DH roof operates in outdoor circulation mode for MOF regeneration, whereas the PV-TC wall operates in indoor circulation mode, utilizing solar photovoltaic thermal energy for the heating and purification of indoor air. During night-time, the system switches to an operational strategy focused on heating and dehumidification: the ventilation openings of the PV-TC wall are closed to form an insulating air layer, whereas the PV-DH roof switches to indoor circulation. In this mode, the radiative cooling effect of the photovoltaic panels is suppressed via physical shielding, and instead, the adsorption heat released during the

MOF adsorption process is employed for the auxiliary heating and dehumidification of the air. The two modules work synergistically with day-night alternation, thereby significantly enhancing the overall thermal contribution of the system. Quantitative calculations indicate that the total winter heat gain of the proposed integrated system is enhanced by 46.8% relative to the single PV-TC wall system. Figure 9b also depicts the variations in relative air humidity at the inlet and outlet of the flow channel. When the outlet humidity is significantly lower than the inlet humidity, it indicates that the system is in the high-efficiency dehumidification stage; conversely, when the outlet humidity is higher than the inlet humidity, it corresponds to the desorption and regeneration process of the MOF adsorption layer. Figure 9c depicts the variation trends of photovoltaic power generation density and ambient irradiance over a two-day period, which exhibit a significant positive correlation, confirming that the system maintains stable photovoltaic conversion capability even under low-irradiance winter conditions. Figure 9d depicts the temporal variations in the formaldehyde concentration at the outlet of the catalytic airflow channel and the corresponding single-pass conversion ratio. After indoor air passes through the α-MnO_2 catalytic layer, the formaldehyde concentration in the treated airflow is reduced, indicating that the PV-TC wall maintains its catalytic purification function under the winter operating conditions considered. These results characterize the formaldehyde-removal performance of the catalytic channel rather than directly quantifying the room-average formaldehyde concentration or occupant exposure reduction.

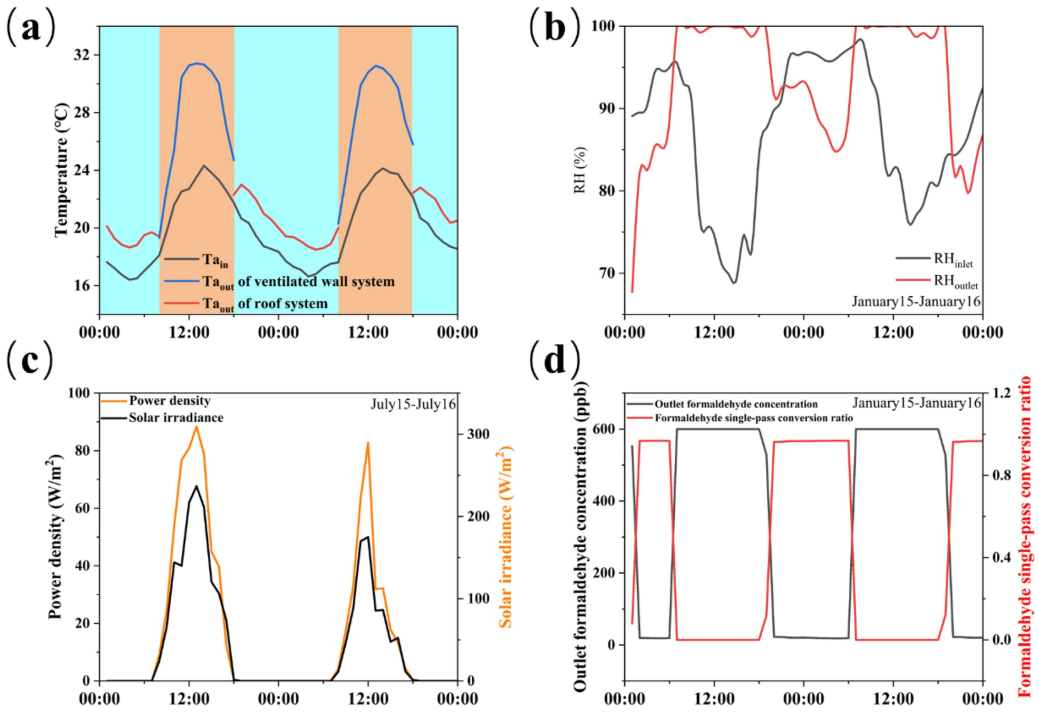


Figure 9. System performance in 15 January to 16 January: (**a**) Variation in air temperature at the inlet and outlet of the airflow channel. (**b**) Variation in air humidity at the inlet and outlet of the airflow channel. (**c**) Variation of photovoltaic panel power generation density. (**d**) Variation in outlet formaldehyde concentration and single-cycle formaldehyde conversion ratio.

We further analyzed the performance of the system throughout the entire month of January. Figure 10a shows the ambient temperature and solar irradiance in Nanjing for January. The ambient temperature fluctuated between −7 °C and 18 °C, with a peak solar irradiance of approximately 687 W/m^2. A significant diurnal temperature variation in the PV panels was observed, with a daytime maximum reaching 40 °C (Figure 10b), demonstrating

the system's effective solar energy collection and photovoltaic thermal conversion capability even under winter sunlight conditions. During winter, the system operates in two separate functional parts. In winter daytime, the PV panels of the PV-TC wall effectively absorb solar radiation, raising their own temperature and that of the air in the flow channel, while the PV panels of the PV-DH roof utilize the absorbed solar thermal energy to provide regeneration conditions for the MOF. At night, to maintain indoor temperature, the ventilation ports of the PV-TC wall are closed to implement indoor thermal insulation. Meanwhile, the MOF in the PV-DH roof achieves dehumidification while releasing adsorption heat, contributing to a slight temperature increase. Throughout January, the prescribed mode sequence yields a continuous supply of heated and dehumidified air, and the model predicts a net heat gain for the envelope; the indoor operative temperature itself was not solved and the room-level heat balance is not represented, so the statement that thermal comfort is maintained cannot be made. Performance data indicate a maximum daily thermal gain of 4065 Wh (Figure 10c), a maximum daily dehumidification capacity of 2.45 L (Figure 10d), a peak PV power generation density of 153 W/m^2 (Figure 10e), and a maximum daily purified air volume of 411 m^3 (Figure 10f).

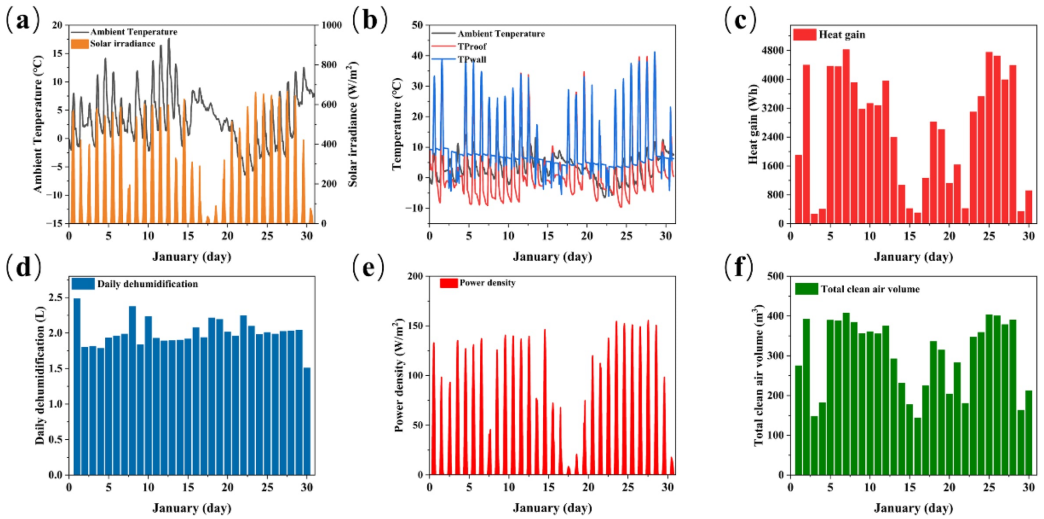


Figure 10. System performance in winter: (**a**) Meteorological parameters in Nanjing in January. (**b**) Comparison of photovoltaic temperature and ambient temperature. (**c**) Daily heating capacity in January. (**d**) Daily dehumidification capacity in January. (**e**) Daily power generation in January. (**f**) Daily clean air production in January.

In summary, the winter simulation results indicate that the system can utilize winter solar energy for partial space heating and for electricity generation, and that the mode-switching sequence can support dehumidification and purification during the night. It should be noted that the heat released at night originates from the moisture taken up by the adsorbent, so the heating contribution depends on the moisture available in the indoor air during the preceding period; where the indoor moisture content is low, as is often the case on winter nights, the adsorption heat available is correspondingly limited and the dehumidification function becomes marginal. This dependence is stated qualitatively here and has not been quantified separately.

4.1.3. Performance Analysis in Transition Season

October was chosen as a representative month to assess the system's performance during the transition season. In Nanjing, indoor cooling constitutes the primary requirement throughout October. Figure 11a illustrates the ambient temperature and solar radiation levels for the month, revealing that the ambient temperature varied between 8.2 °C and

27.3 °C, with a peak solar irradiance of 804 W/m^2. The system's performance during the transition season is depicted in Figure 11. The PV modules efficiently absorb solar thermal energy during daylight hours and deliver radiative cooling during the night-time. On 6 October, the temperature of the PV modules reached 54.8 °C. Figure 11c–f present the system's cooling performance, dehumidification capacity, power generation density, and CADR during the transition season. Figure 11c demonstrates the system's passive cooling capacity, indicating that the system also exhibits superior performance during the transition season. Figure 11d illustrates the system's dehumidification capacity, where the outlet humidity ratio remained below the inlet value on every simulated day of October, that is, the system operated in dehumidification mode; the indoor humidity itself was not solved, and the claim that a comfortable range was maintained is therefore not supported by the present model. Figure 11e shows the system's power generation capacity, while Figure 11f presents the daily clean air output of the PV-TC wall system, indicating high efficiency in indoor air purification. The system achieved a maximum daily radiative cooling gain of 856 Wh, a maximum daily dehumidification capacity of 3.24 L, and a peak daily clean air flow rate of 1063.4 m^3.

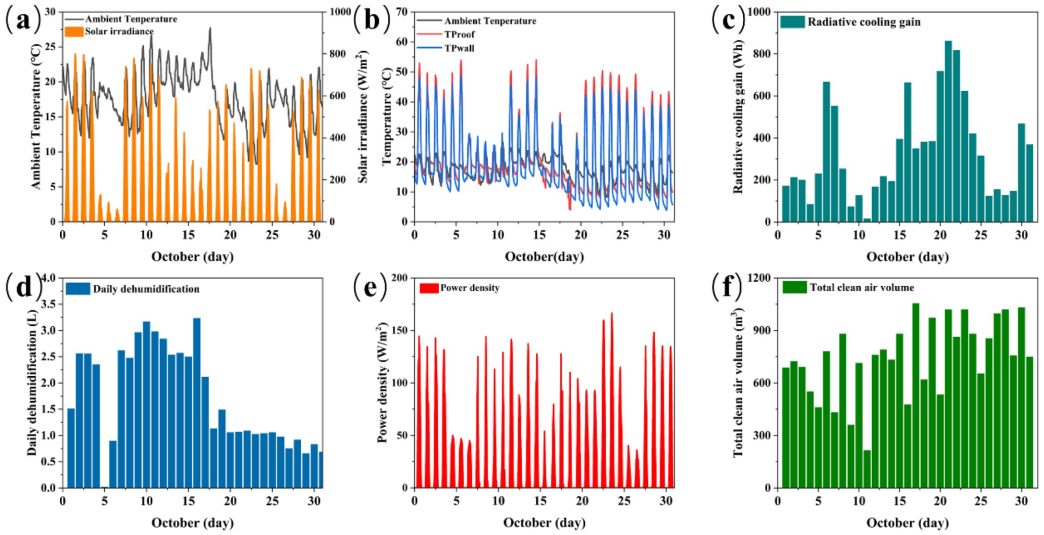


Figure 11. System performance in transition season: (**a**) Meteorological parameters in Nanjing in October. (**b**) Comparison of photovoltaic temperature and ambient temperature. (**c**) Daily cooling capacity in October. (**d**) Daily dehumidification capacity in October. (**e**) Daily power generation in October. (**f**) Daily clean air production in October.

4.2. Annual Performance Analysis of the System

To evaluate the annual heating, cooling, dehumidification, power generation, and formaldehyde degradation performance of the PV-TC/DH hybrid system in different geographical regions, four representative cities—Beijing, Nanjing, Shenzhen, and Xining—were selected. The specific locations, climatic characteristics, as well as the heating and cooling seasons of these four cities are detailed in Table 5. The annual temperature profiles for these cities are shown in Figure 12. Due to variations in sunrise and sunset times at these locations, the forced external circulation hours (for MOF regeneration and daytime photovoltaic operation) are set from 9:00 AM to 5:00 PM for Beijing, Nanjing, and Shenzhen, and from 10:00 AM to 6:00 PM for Xining. During the remaining hours (i.e., night-time), the system automatically switches to internal circulation mode. The annual totals presented in Table 6 are integrated over the full 24 h cycle, accounting for both the daytime external circulation and the night-time internal circulation. The annual totals in Table 6 are accumulated from the operating sequences described in Section 2.2: the solar-driven daytime modes are evalu-

ated over the daylight window given above, whereas the radiative-cooling and adsorption modes are evaluated over the remaining hours. The totals therefore represent the sum of the useful outputs of each mode rather than a continuous 24 h rating. Under consecutive cloudy days, or when the outdoor humidity remains high for prolonged periods, both the thermal driving force for regeneration and the radiative cooling potential are reduced; such periods are not treated separately in the simulation, and the corresponding outputs should be regarded as conditioned by the typical meteorological year adopted. Unless otherwise stated, the annual results in Table 6 refer to the reference configuration defined in Section 3.5, whereas the optimization results reported in Section 4.3 are daily values obtained for the optimized configurations under a typical summer day.

Table 5. Locations and climate features of the four cities.

City	Location	Climate	Heating Season	Cooling Season
Beijing	Northern China (40° N, 116° E)	Temperate semi-humid and arid	November–March	June–September
Nanjing	Eastern China (32°N, 118°E)	Subtropical humid (hot-humid summers)	December–February	June–September
Shenzhen	Southeast China (22° N, 114° E)	Subtropical monsoon	-	May–October
Xining	Northwest China (36° N, 101° E)	Plateau continental	October–April	July–August

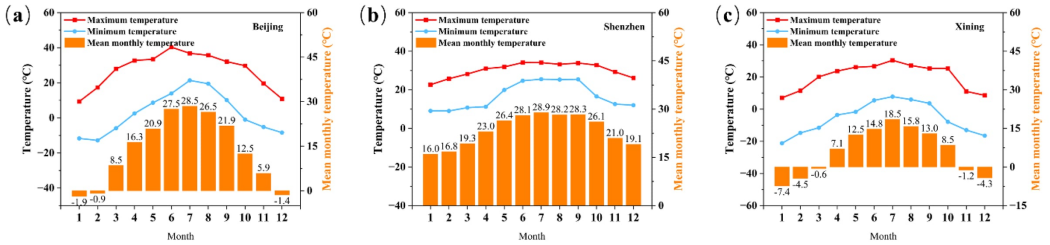


Figure 12. Monthly maximum temperature, monthly minimum temperature and monthly mean temperature of different cities. (**a**) Meteorological parameters of Beijing. (**b**) Meteorological parameters of Shenzhen. (**c**) Meteorological parameters of Xining.

Table 6. Summary Table of Mixed System Benefits in Different Cities.

City	Annual Total Power Generation	Annual Total Dehumidification Capacity (L)	Annual Total Heat Gain (kWh)	Annual Total Cooling Capacity (kWh)	Annual Total Clean Air Volume (m^3)
Beijing	5816	924	1005	667	297,317
Nanjing	4532	1227	665	600	276,129
Shenzhen	5866	1193	326	1002	315,211
Xining	6637	596	2531	135	366,967

Clean-air delivery is defined as the equivalent clean-air volume returned to the occupied space; the hours of the external-circulation mode, in which the treated air is discharged outdoors, are not a delivery to the indoor environment. In the totals reported here the integration was nevertheless performed over the whole cycle, so the annual clean-air volumes in Table 6 include hours of outdoor discharge and are an upper bound; a mode-resolved accounting, and the exclusion of the air exhausted outdoors, have not been carried out. The inlet concentration of 600 ppb is likewise applied to the air treated in every mode, including the outdoor air drawn in during the daytime.

The annual aggregated data are presented in Table 6, which clearly reveals the decisive influence of climatic conditions on the system's various functions. Regarding total annual power generation, Xining leads with 6637 kWh, primarily due to its high altitude, thin air,

and strong solar radiation, which allow the PV modules to receive higher effective irradiance and achieve greater generation efficiency.

The annual dehumidification totals of the reference configuration depend on the number of adsorption hours and on the moisture content of the air treated in each mode. They are not compared between the four cities here, because the daily values reported in Section 4.1 and the annual totals in Table 6 are accumulated over different periods and have not been reconciled; a city-by-city ranking would require a consistent integration of the same quantity and is therefore not drawn.

In terms of thermal management performance, varying demands in different cities lead to differing system output emphases. The total annual thermal gain reaches a remarkable 2531 kWh in Xining, far exceeding that of other cities. This aligns with its long, cold heating season and abundant solar resources, where the system's heating benefits during winter daytime operation are extremely significant. Conversely, the total annual cooling capacity is highest in Shenzhen (1002 kWh), corresponding to its hot summers, as the system provides considerable free cooling for the building through its radiative cooling mode at night.

Regarding total annual clean air delivery, Xining (366,967 m^3) and Shenzhen (315,211 m^3) show the largest volumes. Since the inlet concentration is fixed at 600 ppb in all four simulations, the difference cannot be attributed to the cleanliness of the ambient air; it reflects the longer daylight window, the higher irradiance and the correspondingly higher catalyst temperature at these two locations, together with the number of hours assigned to each mode. The outputs for Beijing and Nanjing are slightly lower but remain of the same order, which indicates that the purification function is active in all four climates; one typical year per city cannot, however, support a claim of universal effectiveness, and the figures should be read as model outputs for the meteorological year adopted.

In summary, the annual simulation results indicate that the relative importance of the different functions varies with climate: the system is dominated by electricity generation and winter heating in the cold and solar-rich conditions of Xining, by dehumidification and cooling in the humid conditions of Nanjing and Shenzhen, and by air purification in all four cities. These annual totals are accumulated over the operating sequences described above and are not season-matched; in particular, thermal gain delivered during the cooling season constitutes a load rather than a benefit, and cooling delivered outside the cooling season is not usable. Season-matched useful energy, and the fraction of the building heating and cooling demand that the system could offset, have not been evaluated and are identified as limitations.

4.3. Multi-Objective Optimization Strategy Analysis

Since the objective of this section is to investigate the optimal configuration under representative summer operating conditions, the optimization was conducted using typical summer meteorological conditions. To investigate the adaptability of the proposed PV-TC/DH hybrid system under different climatic conditions, a multi-objective optimization analysis was conducted based on four representative cities in China, including Nanjing, Beijing, Shenzhen, and Xining. These cities represent different climate characteristics, including subtropical humid with hot-humid summers, cold, hot-summer and warm-winter, and cold-dry plateau conditions, respectively. The optimization strategy was applied to identify the optimal system configuration under different meteorological environments. It should be emphasized that the optimization is performed for a typical summer day, and that both the objective values used in the optimization and those reported in Table 7 are daily quantities for that period. They are not annual indicators, and the climate-adaptive conclusions drawn from them refer to the summer design condition of each city; the design variables also affect the winter modes, which are not included in the optimization. An

extension of the objective functions to annual or multi-season formulations has not been attempted here.

Table 7. Comparison of single-objective optimization, multi-objective optimization, and Unoptimized solutions.

Row	Multi Objective Compromise	Max PV	Max Clean Air	Max Dehumidification	Baseline
Thickness of the air channel of the f Wall (m)	0.015	0.015	0.020	0.015	0.020
Thickness of the air channel of the f Roof (m)	0.040	0.060	0.070	0.040	0.040
Thickness of the MOF (m)	0.006	0.003	0.006	0.006	0.003
Air volume flow (m^3/s)	0.024	0.021	0.024	0.024	0.012
PV coverage of the Wall	0.600	0.900	0.200	0.700	0.600
PV coverage of the Roof	0.400	0.900	0.400	0.300	0.600
Electrical output (kWh)	19.555	33.633	11.011	20.060	22.730
Clean air delivery (m^3)	1041.897	333.586	1461.409	851.787	717.909
Dehumidification (kg)	0.459	0.037	0.267	0.529	0.046
TOPSISS core	0.611	0.424	0.496	0.600	0.341

Significant differences in solar availability and thermal environments were observed among these cities, resulting in different energy conversion and environmental regulation potentials. The solar radiation intensity directly affects photovoltaic electricity generation and thermal energy availability for catalytic purification and MOF regeneration. Meanwhile, ambient temperature and humidity conditions influence the adsorption/desorption behavior of MOF materials and the overall dehumidification performance.

Among the four cities, the variation in solar radiation leads to different optimization requirements for the PV-TC/DH hybrid system. Regions with higher solar availability provide greater potential for photovoltaic electricity generation and daytime thermal regeneration of MOF materials. In contrast, cities with relatively lower solar radiation require more effective utilization of available solar energy through optimization of airflow configuration, PV coverage ratio, and functional material parameters.

The climatic differences also influence the balance among the three optimization objectives, including photovoltaic electricity generation, clean air production, and dehumidification capacity. For humid cities such as Shenzhen and Nanjing, moisture regulation becomes a more dominant requirement due to higher ambient humidity levels, and the optimization strategy tends to enhance moisture adsorption capacity and airflow utilization. For colder and drier cities such as Beijing and Xining, the optimization focuses more on improving solar energy utilization and maintaining sufficient thermal input for system regeneration.

Therefore, although the same optimization framework was applied to all four cities, the obtained Pareto-optimal solutions exhibit different characteristics due to variations in solar radiation, temperature, and humidity conditions. The multi-objective optimization strategy enables the PV-TC/DH hybrid system to achieve climate-adaptive operation by balancing energy generation and indoor environmental regulation under diverse climatic conditions.

4.3.1. Optimization Results

The multi-objective optimization results of the proposed PV-TC/DH hybrid system under four representative cities, including Nanjing, Beijing, Xining, and Shenzhen, are presented in Figure 13. The Pareto fronts obtained using the NSGA-II algorithm are shown, where each point represents a feasible system configuration with different trade-offs among photovoltaic electricity generation, clean air production, and dehumidification capacity.

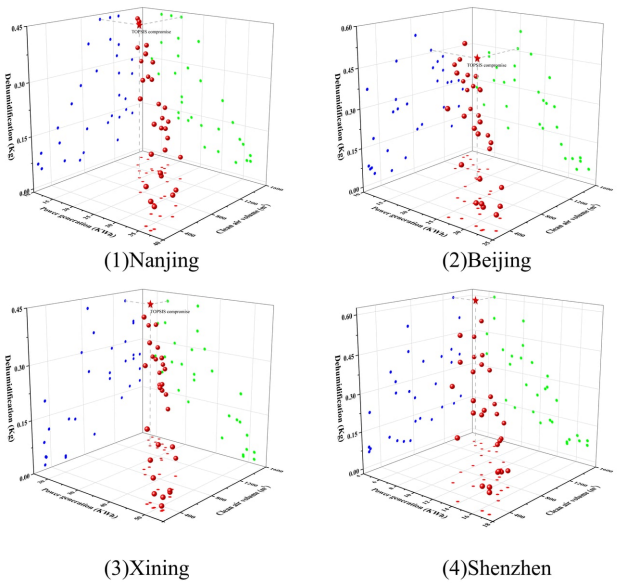


Figure 13. Pareto frontiers of four cities generated based on multi-objective optimization.

The distribution characteristics of the Pareto solutions indicate significant conflicts among the three optimization objectives. The three objectives cannot reach their maximum values simultaneously, and the Pareto front provides a series of compromise solutions between energy generation and indoor environmental regulation.

The optimization results show that climatic conditions have a significant influence on the optimal system performance. Solar radiation intensity determines the available solar energy input, which directly affects photovoltaic electricity generation and the regeneration capability of MOF materials. Among the four cities, Xining achieved the highest photovoltaic electricity generation due to its favorable solar resource conditions. The TOPSIS compromise solution in Xining provided a PV output of 23.52 kWh, which was higher than those in Nanjing (19.56 kWh), Beijing (19.71 kWh), and Shenzhen (6.64 kWh). This indicates that regions with abundant solar resources have greater potential for photovoltaic energy utilization.

In contrast, humid climatic conditions enhance the importance of moisture regulation. Shenzhen and Nanjing, characterized by higher summer humidity, obtained relatively higher dehumidification performance. The TOPSIS compromise solutions achieved dehumidification capacities of 0.603 kg and 0.459 kg, respectively, while Xining and Beijing achieved 0.424 kg and 0.436 kg. The difference reflects the larger number of adsorption hours available in these two cities rather than a demonstrated humidity preference of the sorbent. The values differ by a few per cent and were obtained from single optimizer runs without replicate or convergence evidence, so they are of the same order as the run-to-run variability of the algorithm; the inference that humid climates favor dehumidification is therefore regarded as provisional.

The influence of key optimization parameters on system performance was further analyzed. The air gap thickness affects the convective heat transfer between the airflow and the PV/MOF functional layers. An excessively large air channel weakens thermal interaction due to reduced heat transfer intensity, which decreases the heat utilization efficiency and affects both PV thermal management and MOF regeneration. Therefore, the optimized solutions in the four cities maintained relatively moderate air gap thicknesses. The selected wall air gap values were mainly within 0.015–0.020 m, while the roof air gap values ranged between 0.03 and 0.05 m, The selection of these values follows from the prescribed bounds rather than from a demonstrated trade-off: fan power and pressure drop are not part of the

objective functions and no pressure-loss calculation was performed, so the optimizer has no incentive to avoid narrow gaps or high flow rates.

The MOF thickness showed a consistent optimization trend among different cities. The TOPSIS solutions selected the maximum MOF thickness (0.006 m) for all four cities, demonstrating that increasing adsorption material capacity is beneficial for improving moisture regulation performance. This result indicates that the dehumidification objective has a strong dependence on the available adsorption capacity, especially under humid summer conditions. Although increasing MOF thickness improves adsorption capacity, further increasing thickness may increase thermal resistance and reduce regeneration efficiency. Therefore, the upper boundary was selected based on practical material thickness limitations.

As noted in Section 3.1, the equilibrium capacity scales linearly with layer thickness when q_max and k_LDF are constant, and the internal diffusion and conduction resistances are omitted; the selection of the upper bound in all four cities is therefore a property of the lumped formulation rather than a physical optimum, and it does not indicate that thicker layers would perform better.

The PV coverage ratio exhibited noticeable differences among the four cities due to different climatic conditions. Increasing PV coverage can improve photovoltaic electricity generation, as observed in the MaxPV solutions, where PV generation reached 33.63 kWh, 36.45 kWh, 51.53 kWh, and 17.07 kWh for Nanjing, Beijing, Xining, and Shenzhen, respectively. However, these configurations resulted in significantly lower clean air production and dehumidification performance. Therefore, the TOPSIS compromise solutions selected moderate PV coverage ratios rather than the maximum PV coverage configuration, achieving a better balance between electrical output and environmental regulation.

Overall, the multi-objective optimization results demonstrate that the optimal configuration of the PV-TC/DH hybrid system is highly dependent on local climatic conditions. The proposed optimization framework enables the system to adapt its design parameters according to solar availability and humidity characteristics, thereby achieving a balanced improvement in renewable electricity generation, air purification, and dehumidification performance. The optimization variables are defined on the module area of each element, and the PV coverage ratio partitions that area between photovoltaic conversion and air treatment rather than adding area: it enters the model through the effective photovoltaic area and the effective coated area used in the module balances. The complete design variables of the compromise solutions obtained for the four cities are not tabulated here; only the resulting objective values are reported, whereas the selected values for Nanjing are given in Table 7.

4.3.2. Comparison of Single-Objective and Multi-Objective Optimization Strategy

To further evaluate the effectiveness of the proposed multi-objective optimization strategy, the performance of the TOPSIS-selected compromise solution was compared with three single-objective optimization strategies, including maximum photovoltaic generation (Max PV), maximum clean air production (Max Clean Air), and maximum dehumidification capacity (Max Dehumidification). The baseline configuration was also included for comparison. The optimization results for Nanjing are summarized in Table 7. The baseline case corresponds to the original design parameters, which are listed in the last column of Table 7 and are evaluated under the same summer conditions as the optimized configurations. It should be noted that the TOPSIS scores of the compromise solution and of the maximum-dehumidification solution are close (0.611 and 0.600) and that the two configurations differ mainly in the allocation of area between the modules; the compromise solution is reported because it also retains a considerably higher clean air delivery.

The weighting coefficients of the TOPSIS step were fixed at equal values and no sensitivity analysis of the weights has been performed; the ranking of the compromise solution would change if, for example, clean-air delivery were weighted more heavily, since the maximum-dehumidification solution obtains an almost identical closeness coefficient. A single optimizer run was made for each city, so solutions of similar score cannot be ranked with confidence.

The results indicate that the single-objective optimization strategies can achieve superior performance in their corresponding target functions; however, this improvement is usually accompanied by significant degradation of other performance indicators. In contrast, the multi-objective optimization strategy provides a balanced solution among photovoltaic electricity generation, clean air production, and dehumidification performance.

For the Max PV strategy, the photovoltaic generation reached 33.63 kWh, which was approximately 71.9% higher than the multi-objective compromise solution (19.56 kWh) and 48.0% higher than the baseline configuration (22.73 kWh). This improvement was mainly achieved by increasing the PV coverage ratios of both the wall and roof modules to 0.9, maximizing the effective photovoltaic area. However, this configuration significantly reduced the environmental regulation performance. The clean air production decreased to only 333.59 m^3, which was approximately 68.0% lower than the multi-objective solution, while the dehumidification capacity decreased to 0.037 kg, representing a reduction of approximately 92.0% compared with the compromise solution. These results demonstrate that maximizing PV coverage alone limits the available area for heat and mass transfer, thereby weakening the air purification and moisture regulation functions.

For the Max Clean Air strategy, the clean air production reached the highest value of 1461.41 m^3, which was approximately 40.3% higher than the multi-objective solution. This improvement was obtained by increasing the airflow rate to 0.024 m^3/s and reducing the wall PV coverage ratio to 0.2, which increased the effective air treatment area. However, the photovoltaic generation decreased significantly to 11.01 kWh, approximately 43.7% lower than the multi-objective solution. Meanwhile, the dehumidification capacity decreased to 0.267 kg, indicating that maximizing air purification does not necessarily improve moisture removal performance.

The Max Dehumidification strategy achieved the highest moisture removal capacity of 0.529 kg, which was approximately 15.2% higher than the multi-objective compromise solution. This configuration adopted the maximum MOF thickness (0.006 m) and maximum night-time airflow rate (0.024 m^3/s) to enhance moisture adsorption and mass transfer. However, the clean air production decreased to 851.79 m^3, approximately 18.2% lower than the multi-objective solution. In addition, the photovoltaic generation was slightly higher (20.06 kWh) but did not provide a significant improvement compared with the compromise solution.

Compared with these single-objective optimization strategies, the multi-objective compromise solution achieved a more balanced performance, with photovoltaic generation of 19.56 kWh, clean air production of 1041.90 m^3, and dehumidification capacity of 0.459 kg. Although it did not achieve the maximum value of any individual objective, it avoided severe performance degradation in other functions. The TOPSIS score of the compromise solution reached 0.611, which was higher than those of Max PV (0.424), Max Clean Air (0.496), Max Dehumidification (0.600), and the baseline configuration (0.341).

These results confirm that the proposed multi-objective optimization strategy can effectively balance the conflicting objectives of renewable electricity generation, air purification, and dehumidification. Unlike single-objective optimization, which tends to improve one performance indicator at the expense of others, the multi-objective strategy provides a practical system configuration with comprehensive performance advantages.

4.4. Economic Study

To assess the techno-economic feasibility of the proposed PV-TC/DH hybrid system, we performed a simplified cost–benefit analysis using simulation data from Nanjing, a representative city of this climate zone. This analysis benchmarks the hybrid system's initial capital expenditure and annual operating savings against a conventional split air-conditioning system coupled with a standalone air purifier—the standard configuration for ensuring indoor thermal comfort and air quality in residential buildings. The hybrid system comprises photovoltaic panels functionalized with an α-MnO_2 catalytic layer and a MIL-101(Cr) metal–organic framework (MOF) layer, a supporting frame, fans, regulators, and a control unit. The full breakdown of total initial capital costs is provided in Table 8. The economic assessment is a static, undiscounted estimate for Nanjing. The avoided cost of grid electricity is evaluated at a tariff of 0.60 CNY per kWh, and all generated electricity is assumed to be self-consumed behind the meter; export to the grid and time-of-use tariffs are not considered. The initial investment corresponds to the collector area of the reference configuration. The conventional benchmark, a split air-conditioning unit together with a standalone air purifier, is represented only through the avoided energy quantities of Table 9 and has not been costed itself.

Table 8. Cost details of proposed hybrid system; Take (1USD = 7.1212 CNY).

Component	Unit Cost (CNY/m^2)	Quantity	Subtotal (CNY)
PV panels (wall + roof)	152	24 m^2	3648
MOF material (MIL-101(Cr))	133	12 m^2	1596
Balance-of-system (fans, ducts, controls)	124	24 m^2	2976
Total	-	-	8220

Table 9. Revenue from various parts of the system; Take (1 USD = 7.1212 CNY).

Savings Category	Annual Quantity	Equivalent Electricity (kWh)	Monetary Savings (CNY/year)
PV electricity generation	4532 kWh	-	2719.2
Cooling load reduction	600 kWh	200 (COP = 3.0)	120
Heating load reduction	665 kWh	266 (COP = 2.5)	159.6
Dehumidification	1227 L	471.2	282.7
Air purification	276,129 m^3	55	33
Total annual savings	-	-	3314.5

About 82% of the monetised saving arises from photovoltaic generation, so the incremental benefit of the catalytic and dehumidification functions relative to a photovoltaic-only envelope is not isolated; such an incremental comparison has not been made. The cooling and heating quantities of Table 9 are credited at the electricity tariff although, as stated in Section 4.2, they are not season-matched and therefore represent energy outputs rather than avoided loads.

Notably, the hybrid system achieves building energy savings through three synergistic mechanisms: (1) On-site electricity generation using photovoltaic modules to offset grid electricity consumption; (2) Reduced cooling and heating loads via passive thermal regulation, namely radiative cooling in summer and passive solar heating in winter; (3) Elimination of dedicated energy use for dehumidification and air purification. Based on annual simula-

tions in Nanjing, we calculated the hybrid system's annual energy and cost savings, yielding a simple payback period of 2.5 years; full results are summarized in Table 9. The payback period quoted here is the simple undiscounted ratio of the initial investment in Table 8 to the annual monetary savings in Table 9. The equivalent electricity for dehumidification corresponds to removing the condensate at a latent heat of about 2.45 MJ per kilogram with an effective electrical coefficient of performance of about 1.8, and the equivalent electricity for air purification to a specific energy consumption of about 0.2 Wh per cubic meter of treated air; both are engineering estimates representative of small-scale domestic equipment rather than values derived from a specific product.

Importantly, this assessment remains preliminary, and several cost items are not included. The initial investment covers the photovoltaic panels, the sorbent coating and the balance of system, but not the catalyst and selective coatings, the supporting frame, the movable cover used on winter nights, installation labor, or the control and instrumentation required for mode switching. Periodic replacement of the sorbent and of the catalyst, the gradual degradation of the photovoltaic output, maintenance of fans and dampers, and the discounting of future savings are likewise omitted, and the conversion of dehumidification and purification output into avoided electricity rests on the engineering estimates stated above. The cost of the sorbent is calculated from the material cost of the MIL-101(Cr) synthesized in our laboratory per unit of coated module area, including the preparation and application of the coating; it therefore excludes the labor and the scale-up of coating production, and it is not comparable with the price of the powder per kilogram. A discounted life-cycle cost analysis, an incremental comparison against a photovoltaic-only or building-integrated photovoltaic baseline, a sensitivity analysis with respect to tariff, material lifetime and maintenance, and a costing of the conventional benchmark are therefore needed before the payback period can be regarded as a reliable estimate.

5. Conclusions

This study proposed and systematically investigated a building-integrated photovoltaic–thermal catalytic-dehumidification (PV-TC/DH) system that achieves energy cascade utilization through a series-connected configuration of a PV-TC wall and a PV-DH roof. By coupling daytime solar energy harvesting with night-time radiative cooling, and by sequentially utilizing PV-generated low-grade thermal energy for thermal catalytic purification, airflow preheating, and subsequent MOF regeneration, the system provides a multifunctional approach for reducing building operational energy demand. The main conclusions are summarized as follows:

(1) The energy cascade design enables effective utilization of low-grade solar thermal energy (~40–60 °C) that would otherwise be wasted. The PV-TC wall utilizes PV-generated thermal energy to establish the operating temperature required for thermal catalytic purification and to preheat the airflow, after which the heated airflow enters the PV-DH roof and contributes to MOF regeneration. At night, radiative cooling lowers the surface temperature of both modules, which raises the equilibrium uptake of the MOF layer; the catalytic layer continues to oxidize formaldehyde at the prevailing temperature, at a rate that varies only weakly with temperature because the fitted activation energy is small. Compared with a standalone PV-DH roof system, the integrated configuration improves cooling capacity by 79.2% and dehumidification capacity by 26.9%, showing that the integrated configuration outperforms the single-module roof system under the conditions compared. It should be noted that the two configurations compared here differ in collector area and airflow, so these percentages describe the configuration-level benefit of the integrated design rather than an area-normalized improvement.

(2) The multi-objective optimization framework identifies compromise configurations that balance the conflicting objectives, but the values are specific to the summer design day and to the prescribed bounds. For Nanjing, the TOPSIS solution delivers 19.56 kWh of photovoltaic generation, 1041.9 m^3 of clean air and 0.459 kg of dehumidification per day, against 22.73 kWh, 717.9 m^3 and 0.046 kg for the baseline configuration and 33.63 kWh, 333.6 m^3 and 0.037 kg for the maximum-PV solution; the TOPSIS closeness coefficient of the compromise solution is 0.611. These values are daily quantities for a typical summer day and are not annual indicators, and the design variables also govern the winter modes, which were not optimized. Because the MOF thickness reaches its upper bound in all four cities and several other variables approach theirs, the climate-dependent preferences should be regarded as provisional until the ranges are widened. No sensitivity analysis of the TOPSIS weights was performed and a single optimizer run per city was made, so the ranking between solutions of similar score is not resolvable. Daily dehumidification in Shenzhen is lower than in Nanjing, and the daily and annual figures are not placed in a common range for that reason.

(3) The reference configuration yields annual photovoltaic generation of 4532 kWh in Nanjing and 6637 kWh in Xining, annual clean-air delivery of 276,129 m^3 and 366,967 m^3, respectively, and an annual thermal gain of 2531 kWh in Xining. These annual totals are accumulated over the prescribed operating sequence without season matching and are therefore energy outputs rather than avoided loads, and the daily and annual accumulations have not been reconciled with each other, so no ranking between cities is drawn from them. The simple payback period of 2.5 years obtained for Nanjing under the assumptions of Section 4.4 is a static estimate that omits several cost items and rests on a sorbent costed at the material cost of in-house synthesis of MIL-101(Cr) at laboratory scale rather than on a commercial quotation for the coated module; it is an order-of-magnitude indication rather than a demonstrated economic case.

It should be noted that the performance presented in this study is based on the selected typical meteorological conditions and the corresponding numerical operating scenarios. Although the results demonstrate the potential of the proposed system for coordinated daytime thermal regeneration and night-time moisture adsorption, its performance under prolonged unfavorable weather conditions, such as consecutive cloudy days, elevated night-time ambient temperatures, and sustained high outdoor humidity, has not been independently quantified. In particular, insufficient daytime solar thermal input may limit MOF regeneration, while unfavorable night-time conditions may reduce the radiative cooling potential and adsorption capacity. The current model simplifies the formaldehyde oxidation pathway by assuming complete conversion to CO_2 and H_2O. The potential generation of intermediate by-products (e.g., CO and formic acid) and the long-term deactivation of the α-MnO_2 catalyst under high-humidity night-time conditions were not independently modeled. Additionally, the downstream MIL-101(Cr) layer may physically adsorb unreacted formaldehyde or VOCs, which was not decoupled from the water-vapor adsorption model. These aspects represent important directions for future experimental and modeling studies to ensure the long-term environmental safety and stability of the proposed system. Future studies should further investigate the operating limits of the system under extreme and consecutive adverse weather conditions and evaluate the long-term stability of the adsorption–desorption cycle through integrated experimental testing. In summary, the proposed PV-TC/DH system is a candidate technology for building envelopes that simultaneously generate renewable electricity, purify indoor air, and regulate humidity without relying on energy-intensive HVAC systems. The energy cascade design and climate-adaptive optimization framework contribute to the growing body of knowledge on building-

integrated renewable energy systems and offer new opportunities for the development of energy-efficient and healthy buildings.

Several limitations should nevertheless be acknowledged. The experimental validation refers to the two modules separately, and no room-level heat and moisture balance was solved, so the results describe the output of the envelope and of the supply air rather than the indoor operative temperature, humidity or occupant exposure; the annual totals are accumulated without season matching and the fraction of building demand offset was not evaluated. In addition, the leaching of Cr(III)/Cr(VI) from MIL-101(Cr) into the supply air and the disposal of spent sorbent, condensation and mold growth on the radiatively cooled cavity surfaces, dust fouling of the optical and coated surfaces, the fire behavior of a ventilated photovoltaic cavity and the noise of the fans and dampers have not been assessed and require dedicated experimental work. The modest optimization budget, the equal TOPSIS weights, the single temperature-coefficient photovoltaic model and the static economic estimate further limit the conclusions, which are therefore model-based estimates of technical potential rather than demonstrated system performance.

Author Contributions: Conceptualization, J.J. and B.Y.; Methodology, N.L. and B.Y.; Software, J.L. and N.L.; Validation, J.L., W.L. and W.W.; Investigation, N.L.; Resources, N.L. and J.J.; Data curation, B.Y.; Writing—original draft, J.L. and W.W.; Writing—review and editing, J.L. and F.Z.; Visualization, J.L., W.L. and F.Z.; Supervision, B.Y.; Project administration, B.Y.; Funding acquisition, N.L., J.J. and B.Y. All authors have read and agreed to the published version of the manuscript.

Funding: This research is supported by the National Natural Science Foundation of China (No. 52508120, No. 52238004), Natural Science Foundation of Jiangsu Province (No. BK20250596).

Data Availability Statement: The data presented in this study are available on request from the corresponding author.

Conflicts of Interest: The authors declare no conflicts of interest.

References

1. González-Torres, M.; Pérez-Lombard, L.; Coronel, J.F.; Maestre, I.R.; Yan, D. A review on buildings energy information: Trends, end-uses, fuels and drivers. *Energy Rep.* **2022**, *8*, 626–637. [CrossRef]
2. Heer, P.; Derungs, C.; Huber, B.; Bünning, F.; Fricker, R.; Stoller, S.; Niesen, B. Comprehensive energy demand and usage data for building automation. *Sci. Data* **2024**, *11*, 469. [CrossRef]
3. Ballif, C.; Perret-Aebi, L.-E.; Lufkin, S.; Rey, E. Integrated thinking for photovoltaics in buildings. *Nat. Energy* **2018**, *3*, 438–442. [CrossRef]
4. Tang, X.; Bai, Y.; Duong, A.; Smith, M.T.; Li, L.; Zhang, L. Formaldehyde in China: Production, consumption, exposure levels, and health effects. *Environ. Int.* **2009**, *35*, 1210–1224. [CrossRef]
5. Plaisance, H.; Blondel, A.; Desauziers, V.; Mocho, P. Characteristics of formaldehyde emissions from indoor materials assessed by a method using passive flux sampler measurements. *Build. Environ.* **2014**, *73*, 249–255. [CrossRef]
6. Chao, Y.; Wang, C.; Zhou, Z.; Yang, X.; Du, Y.; Liang, Y.; Deng, N.; Liu, J. Recent advance of adsorbent materials for indoor dehumidification. *Sep. Purif. Technol.* **2025**, *357*, 130096. [CrossRef]
7. Zhou, X.; Zhang, Y.; Huo, G.; Zhang, Z.; Xin, J.; Kang, S.; Wang, Z.; Li, N. Rationally designed fluorinated aromatic polyamide membrane for stable air dehumidification. *J. Membr. Sci.* **2023**, *687*, 122042. [CrossRef]
8. Ge, F.; Wang, C. Exergy analysis of dehumidification systems: A comparison between the condensing dehumidification and the desiccant wheel dehumidification. *Energy Convers. Manag.* **2020**, *224*, 113343. [CrossRef]
9. Bianfeng, Y.; Cong, W.; Ji, X.; Yuan, Y.; Yingxu, C.; Junneng, N. Solar regenerated carbon-based composite desiccant coated heat exchangers for air dehumidification. *Energy* **2024**, *299*, 131537. [CrossRef]
10. Fix, A.J.; Oh, J.; Braun, J.E.; Warsinger, D.M. Dual-module humidity pump for efficient air dehumidification: Demonstration and performance limitations. *Appl. Energy* **2024**, *360*, 122771. [CrossRef]
11. Liang, C.; Li, X.; Shi, W. Humidity grade-matched fresh air dehumidification system with adjustable treating stages. *J. Clean. Prod.* **2023**, *423*, 138822. [CrossRef]

12. Akhtar, M.U.S.; Fadlallah, S.O.; Khan, M.I.; Asfand, F.; Al-Ghamdi, S.G.; Mishra, R. Sustainable humidity control in the built environment: Recent research and technological advancements in thermal driven dehumidification systems. *Energy Build.* **2024**, *304*, 113846. [CrossRef]
13. Guo, J.; Bilbao, J.I.; Sproul, A.B. A novel solar cooling cycle—A ground coupled PV/T desiccant cooling (GPVTDC) system with low heat source temperatures. *Renew. Energy* **2020**, *162*, 1273–1284. [CrossRef]
14. Huang, M.; Yang, R.; Tang, G.H.; Pu, J.H.; Sun, Q.; Du, M. Quantifying the effects of dust characteristics on the performance of radiative cooling PV systems. *Appl. Energy* **2025**, *377*, 124672. [CrossRef]
15. Yu, B.; He, W.; Li, N.; Yang, F.; Ji, J. Thermal catalytic oxidation performance study of SWTCO system for the degradation of indoor formaldehyde: Kinetics and feasibility analysis. *Build. Environ.* **2016**, *108*, 183–193. [CrossRef]
16. Zong, C.; Li, H.; Zheng, L.; Song, W. Evaluation and optimization of a new condensation dehumidification system with fan-coil units using low-cost cold source for greenhouses. *J. Clean. Prod.* **2023**, *433*, 139805. [CrossRef]
17. Bevilacqua, P.; Benevento, F.; Bruno, R.; Arcuri, N. Are Trombe walls suitable passive systems for the reduction of the yearly building energy requirements? *Energy* **2019**, *185*, 554–566. [CrossRef]
18. Yu, B.; Li, N.; Xie, H.; Ji, J. The performance analysis on a novel purification-cleaning trombe wall based on solar thermal sterilization and thermal catalytic principles. *Energy* **2021**, *225*, 120275. [CrossRef]
19. Su, W.; Lu, Z.; She, X.; Zhou, J.; Wang, F.; Sun, B.; Zhang, X. Liquid desiccant regeneration for advanced air conditioning: A comprehensive review on desiccant materials, regenerators, systems and improvement technologies. *Appl. Energy* **2022**, *308*, 118394. [CrossRef]
20. Rafique, M.M.; Gandhidasan, P.; Bahaidarah, H.M.S. Liquid desiccant materials and dehumidifiers—A review. *Renew. Sustain. Energy Rev.* **2016**, *56*, 179–195. [CrossRef]
21. Li, Y.; Yu, B.; Li, N. The performance analysis of a novel manganese oxide solar low-temperature thermal-catalyst in building multifunctional applications. *Energy Build.* **2023**, *297*, 113477. [CrossRef]
22. Che, L.; Yu, B.; Li, N.; Ji, J. The performance analysis of porous adsorbent supported thermal catalysts: Low-temperature catalysis and building integrated multifunctional application. *J. Build. Eng.* **2024**, *85*, 108613. [CrossRef]
23. Wu, H.; Li, N.; Zhang, G.; Zhang, G.; Ji, J.; Yu, B. Performance analysis on a wood-color thermal catalytic Trombe wall in wood buildings. *Energy Build.* **2024**, *308*, 114034. [CrossRef]
24. Li, N.; Cao, X.; Zhang, G.; Wang, Y.; Hu, X.; Liu, J.; Yu, B.; Ji, J.; Liu, X. The experimental and numerical study on a novel all-day PCM thermal-catalytic purified Trombe wall in winter. *Energy* **2024**, *299*, 131397. [CrossRef]
25. Xu, F.; Wu, H.; Zhao, B.; Ji, J.; Li, N.; Yu, B. A novel solar photothermal/radiative cooling-thermal catalytic (PT/RC-TC) hybrid system for improving indoor environment by a broadband absorber/emitter with thermal catalysts. *Energy Build.* **2025**, *327*, 115097. [CrossRef]
26. Moayed Mohseni, M.; Jouyandeh, M.; Mohammad Sajadi, S.; Hejna, A.; Habibzadeh, S.; Mohaddespour, A.; Rabiee, N.; Daneshgar, H.; Akhavan, O.; Asadnia, M.; et al. Metal-organic frameworks (MOF) based heat transfer: A comprehensive review. *Chem. Eng. J.* **2022**, *449*, 137700. [CrossRef]
27. Zhang, X.; Li, C.; Chinnappan, A.; Zheng, S.; Sun, Z.; Baskar, C.; Ramakrishna, S. MOFs for handling latent load in air cooling: From moisture adsorption and optimization to application as heat exchanger coatings in air conditioners. *Coord. Chem. Rev.* **2023**, *495*, 215384. [CrossRef]
28. Vivekh, P.; Cheng, G.G.; You, G.L.; Zhang, H.L.; Bui, T.D. Unveiling the water sorption kinetics, thermodynamics, and air dehumidification performance of sustainably synthesized metal–organic frameworks. *Therm. Sci. Eng. Prog.* **2024**, *54*, 102855. [CrossRef]
29. Cui, S.; Qin, M.; Marandi, A.; Steggles, V.; Wang, S.; Feng, X.; Nouar, F.; Serre, C. Metal-Organic Frameworks as advanced moisture sorbents for energy-efficient high temperature cooling. *Sci. Rep.* **2018**, *8*, 15284. [CrossRef]
30. Ding, D.; Qin, M. Comparative study of Metal-Organic frameworks (MOFs) for indoor moisture control. *Appl. Therm. Eng.* **2024**, *257*, 124329. [CrossRef]
31. Zhang, B.; Zhu, Z.; Wang, X.; Liu, X.; Kapteijn, F. Water Adsorption in MOFs: Structures and Applications. *Adv. Funct. Mater.* **2024**, *34*, 2304788. [CrossRef]
32. Shahvari, S.Z.; Clark, J.D. Approaching theoretical maximum energy performance for desiccant dehumidification using staged and optimized metal-organic frameworks. *Appl. Energy* **2023**, *331*, 120421. [CrossRef]
33. Che, L.; Li, N.; Wei, W.; Li, J.; Ji, J.; Zhao, X.; Yu, B.; Wang, Q. Day-Night energy harvesting: Photovoltaics-driven moisture evaporation and absorption for simultaneous 24-hour power and dehumidification. *Innov. Energy* **2025**, *2*, 100078. [CrossRef]
34. Hu, M.; Zhao, B.; Li, J.; Wang, Y.; Pei, G. Preliminary thermal analysis of a combined photovoltaic–photothermic–nocturnal radiative cooling system. *Energy* **2017**, *137*, 419–430. [CrossRef]
35. Marion, B.; Smith, B. Photovoltaic system derived data for determining the solar resource and for modeling the performance of other photovoltaic systems. *Sol. Energy* **2017**, *147*, 349–357. [CrossRef]

36. Suhendri, S.; Hu, M.; Dan, Y.; Su, Y.; Zhao, B.; Riffat, S. Building energy-saving potential of a dual-functional solar heating and radiative cooling system. *Energy Build.* **2024**, *303*, 113764. [CrossRef]
37. Hu, M.; Zhao, B.; Suhendri; Cao, J.; Wang, Q.; Riffat, S.; Su, Y.; Pei, G. Extending the operation of a solar air collector to night-time by integrating radiative sky cooling: A comparative experimental study. *Energy* **2022**, *251*, 123986. [CrossRef]
38. Yu, B.; He, W.; Li, N.; Wang, L.; Cai, J.; Chen, H.; Ji, J.; Xu, G. Experimental and numerical performance analysis of a TC-Trombe wall. *Appl. Energy* **2017**, *206*, 70–82. [CrossRef]
39. Pei, J.; Han, X.; Lu, Y. Performance and kinetics of catalytic oxidation of formaldehyde over copper manganese oxide catalyst. *Build. Environ.* **2015**, *84*, 134–141. [CrossRef]
40. Naidu, H.; Mathews, A.P. Linear driving force analysis of adsorption dynamics in stratified fixed-bed adsorbers. *Sep. Purif. Technol.* **2021**, *257*, 117955. [CrossRef]
41. Wang, Y.; Ji, J.; Sun, W.; Yuan, W.; Cai, J.; Guo, C.; He, W. Experiment and simulation study on the optimization of the PV direct-coupled solar water heating system. *Energy* **2016**, *100*, 154–166. [CrossRef]
42. Hu, M.; Zhao, B.; Ao, X.; Su, Y.; Pei, G. Numerical study and experimental validation of a combined diurnal solar heating and nocturnal radiative cooling collector. *Appl. Therm. Eng.* **2018**, *145*, 1–13. [CrossRef]
43. Fernández-Hernández, F.; Cejudo-López, J.M.; Domínguez-Muñoz, F.; Carrillo-Andrés, A. A new desiccant channel to be integrated in building façades. *Energy Build.* **2015**, *86*, 318–327. [CrossRef]
44. Yu, B.; Jiang, Q.; He, W.; Hu, Z.; Chen, H.; Ji, J.; Xu, G. The performance analysis of a novel TC-Trombe wall system in heating seasons. *Energy Convers. Manag.* **2018**, *164*, 242–261. [CrossRef]
45. Wang, J.; Guo, X. Adsorption kinetic models: Physical meanings, applications, and solving methods. *J. Hazard. Mater.* **2020**, *390*, 122156. [CrossRef]
46. Mohamad Shirajuddin, T.; Muhammad, N.S.; Abdullah, J. Optimization problems in water distribution systems using Non-dominated Sorting Genetic Algorithm II: An overview. *Ain Shams Eng. J.* **2023**, *14*, 101932. [CrossRef]
47. Ben Seddik, Z.; Ben Taher, M.A.; Laknizi, A.; Ahachad, M.; Bahraoui, F.; Mahdaoui, M. Hybridization of Taguchi method and genetic algorithm to optimize a PVT in different Moroccan climatic zones. *Energy* **2022**, *250*, 123802. [CrossRef]
48. Hosouli, S.; Gaikwad, N.; Qamar, S.H.; Gomes, J. Optimizing photovoltaic thermal (PVT) collector selection: A multi-criteria decision-making (MCDM) approach for renewable energy systems. *Heliyon* **2024**, *10*, e27605. [CrossRef]
49. Wu, H.; Li, Y.; Ji, J.; Huang, W.; Zhao, X.; Yu, B.; Li, N. The running modes and building application performance on a solar-based thermal catalytic purification module with PCM for 24-h heating and air purification. *Energy Build.* **2025**, *331*, 115372. [CrossRef]
50. Liu, F.; Rong, S.; Zhang, P.; Gao, L. One-step synthesis of nanocarbon-decorated MnO2 with superior activity for indoor formaldehyde removal at room temperature. *Appl. Catal. B Environ.* **2018**, *235*, 158–167. [CrossRef]
51. Chen, J.; Tang, H.; Huang, M.; Yan, Y.; Zhang, J.; Liu, H.; Zhang, J.; Wang, G.; Wang, R. Surface lattice oxygen activation by nitrogen-doped manganese dioxide as an effective and longevous catalyst for indoor HCHO decomposition. *ACS Appl. Mater. Interfaces* **2021**, *13*, 26960–26970. [CrossRef]

Disclaimer/Publisher's Note: The statements, opinions and data contained in all publications are solely those of the individual author(s) and contributor(s) and not of MDPI and/or the editor(s). MDPI and/or the editor(s) disclaim responsibility for any injury to people or property resulting from any ideas, methods, instructions or products referred to in the content.